Agricultural Water Management 288 (2023) 108472

Contents lists available at ScienceDirect

Agricultural Water Management

journal homepage: www.elsevier.com/locate/agwat

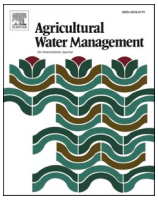

Field-scale assessment of soil water dynamics using distributed modeling and electromagnetic conductivity imaging

Tiago B. Ramos [a,*], Ana R. Oliveira [a], Hanaa Darouich [b], Maria C. Gonçalves [c], Francisco J. Martínez-Moreno [d], Mario Ramos Rodríguez [e], Karl Vanderlinden [e], Mohammad Farzamian [c]

[a] Centro de Ciência e Tecnologia do Ambiente e do Mar (MARETEC–LARSyS), Instituto Superior Técnico, Universidade de Lisboa, Av. Rovisco Pais, 1, 1049-001 Lisboa, Portugal
[b] LEAF—Linking Landscape, Environment, Agriculture and Food Research Center, Associated Laboratory TERRA, Instituto Superior de Agronomia, Universidade de Lisboa, Tapada da Ajuda, 1349-017 Lisboa, Portugal
[c] Instituto Nacional de Investigação Agrária e Veterinária, Avenida da República, Quinta do Marquês, 2780-157 Oeiras, Portugal
[d] Departamento de Geodinámica, Estratigrafía y Paleontología. Universidad Complutense de Madrid, 28040 Madrid, Spain
[e] IFAPA Centro Alameda del Obispo, 14004 Córdoba, Spain

ARTICLE INFO

Handling Editor - Dr. B.E. Clothier

Keywords:
Irrigation water management
Pedotransfer functions
Soil water balance
Soil variability
Three-dimensional modeling

ABSTRACT

Knowledge of the soil water balance is fundamental for improving crop water use in agricultural fields. Estimates are normally for representative and homogeneous areas where the variability of soil properties is neglected. However, this variability significantly impacts soil water dynamics at the field scale. In this study, the MOHID-Land distributed process-based model was used to compute the spatially explicit soil water dynamics in a 22.6-ha almond field located in southern Portugal. An electromagnetic induction survey was first performed to obtain electromagnetic images of the real soil conductivity in depth, which were related to soil texture. Then, pedotransfer functions were used to convert soil texture into soil hydraulic data. MOHID-Land results included maps of the spatial distribution of soil water contents, actual crop transpiration, actual soil evaporation, percolation below the rootzone, and surface runoff. These allowed identifying preferential flow pathways as well as the main control factors influencing soil water dynamics at the field scale. Some development needs were identified, and overcoming them would enhance the significance of contributions such as this study to the field of precision agriculture.

1. Introduction

Agriculture, especially irrigation, is responsible for 70% of all freshwater withdrawals in the world, and for as much as 90% in the least developed regions (UNESCO, 2020). It is also a key promoter of important land degradation processes, namely by contributing to the contamination or depletion of water resources, promoting soil erosion and soil salinization, being also associated with biodiversity loss (Pereira et al., 2009). The literature therefore consistently advocates the need to improve agricultural water management at the field scale. In most cases, this involves implementing measures and practices to restrict the use of water, control non-beneficial water consumption, and protect the environment. Such objectives are typically achieved by considering representative areas of the field with similar soil and crop conditions (Pereira et al., 2020a; Šimůnek et al., 2016, 2008; van Dam et al., 2004). However, soil properties, particularly soil hydraulic properties (SHP), are known to show significant spatial and temporal variability due to short-range variability in the pore system, and precipitation, wind and moisture fluxes across the field. They are also impacted by the variability in agricultural management practices within the field, the variability of land surface geomorphic features, and variability in land surface ecology (Vereecken et al., 2007).

Understanding the spatio-temporal dynamics of hydrological fluxes in soils requires detailed information on the variability of SHP but is usually limited by lack of data. The characterization of these properties beyond the local scale remains a key challenge in soil hydrology (Vereecken et al., 2022). Direct characterization of SHP is costly, time-consuming and involves methods that are impractical for

* Corresponding author.
E-mail addresses: tiagobramos@tecnico.ulisboa.pt, tiago_ramos@netcabo.pt (T.B. Ramos).

https://doi.org/10.1016/j.agwat.2023.108472
Received 25 May 2023; Received in revised form 1 August 2023; Accepted 2 August 2023
Available online 4 August 2023

large-scale applications requiring many samples to quantify the spatial and temporal variability of soil-water processes. Electromagnetic induction (EMI) can serve as a viable alternative to such direct methods. It offers a rapid, repeatable, accurate and non-invasive approach to characterizing the spatial variability of soil properties over large areas at relatively low cost.

EMI measures the apparent electrical conductivity (EC_a) of soil over a given volume of the soil subsurface and can be used as an approximation for soil properties. This involves the establishment of location-specific relationships between the EC_a and soil properties (Allred et al., 2008; Doolittle and Brevik, 2014; Jayawickreme et al., 2014). Examples can be found for soil moisture (Martinez et al., 2018; Huang et al., 2016), particle size distribution (Kelley et al., 2017; Huang et al., 2014), cation exchange capacity (Triantafilis et al., 2009) and soil salinity (Paz et al., 2020; Corwin and Lesch, 2005). However, a reliable relationship between EC_a and SHP data remains elusive due to the difficulty in accurately portraying the non-linear behavior of SHP. Dragonetti et al. (2022) is a rare example where the soil hydraulic parameters of the Mualem-van Genuchten functional relationships (Mualem, 1976; van Genuchten, 1980) were estimated from inverse modeling of EMI data collected during an infiltration experiment, but with limited application to large areas.

Another interesting topic of research is the incorporation of EMI data into the development and use of pedotransfer functions (PTFs) as proposed by Mohanty (2013), which to our knowledge has not been fully explored. Nowadays, several PTFs exist relating SHP with basic soil properties using different mathematical approaches, as reviewed by Van Looy et al. (2017). An early example of an application of PTFs using soil basic data derived from EMI survey was given by Wallor et al. (2019). In this study, the authors employed a one-dimensional (1D) model to simulate soil water and nutrient fluxes as well as crop yields in 60 locations spread across a 22-ha field in Germany. Subsequently, the results were interpolated over the entire field. Similarly, Brogi et al., (2019, 2020, 2021) conducted an EMI survey to obtain a high-resolution soil map of a 1 km^2 area in Germany. Afterwards, soil water dynamics, crop growth, and yields were simulated at multiple locations using 1D agroecosystem modeling, with the SHP derived from PTFs and the surveyed soil basic data. These studies defined management zones based on the EMI inputs, which were then used for modeling soil water and crop growth processes. However, they did not fully capture the within-field variability of agricultural fields and hydrological fluxes.

Following the same reasoning, high resolution digital SHP maps of agricultural fields can be developed from EMI data collected during surveys, the established relationships to basic soil data, and regional PTFs. They can then feed the need of distributed modeling tools capable of simulating the spatio-temporal dynamics of hydrological fluxes in soil at the field scale. Fully distributed models compute the soil water fluxes in a three-dimensional (3D) grid using Richards' equation, taking into account vertical and lateral interactions between cells in the simulated domain (Fatichi et al., 2016). The accurate representation of the spatial variability of SHP is crucial for the reliability of the model simulations. The resolution of the model simulations depends on the details of the EMI survey and computational capabilities. The immediate result is an insight into the spatio-temporal variability of the different components of the soil water balance, namely actual evapotranspiration, surface and subsurface runoff, soil moisture, and infiltration, with a level of detail that can hardly be obtained from satellite or unmanned aerial vehicles measurements. Of course, the validation of such results is a challenge in itself, but the results would allow going further than simply identifying areas that are more suitable to crop growth, i.e., soil or irrigation management zones, as is currently done (Nawar et al., 2017). Wallor et al. (2019) and Brogi et al., (2020, 2021) have already demonstrated what is considered the most effective approach for managing these management zones, i.e., through integration of modeling to enhance crop production. With distributed three-dimensional modeling, it also becomes possible to identify preferred flow paths at the field scale, which would contribute to minimizing nutrient and contaminant losses.

The objectives of this study are: (i) to assess EC_a across a 22.6 ha almond field; (ii) to establish a relationship between the surveyed EC_a and soil texture data; (iii) to derive high resolution maps of soil texture for different soil layers of the study field; (iv) to upgrade the soil texture maps to digital maps of SHP and use them as input to a fully distributed three-dimensional soil hydrological model; and (v) to simulate the spatial variability of soil water balance components over two growing seasons. During the development of this study, limitations in the approach became clear. These limitations are discussed in detail, while further research needs are identified to make the approach more feasible and relevant for precision agriculture applications.

2. Material and methods

2.1. Description of the study field

This study was performed on a 22.6-ha almond field in Montes Velhos, southern Portugal (37.94° N, 8.15° W, 111 m a.s.l.) from January 1st, 2019 to December 31st, 2020 (Fig. 1). The climate in the region is classified as semi-arid. The mean annual air temperature is 16.3 °C, ranging from a minimum of 9.8 °C in January to a maximum of 23.1 °C in August. The mean annual precipitation is 454 mm, concentrated mainly between October and May. The mean annual reference evapotranspiration (ET_o) computed using the FAO56 Penman-Monteith (PM) equation (Allen et al., 1998) is 1363 mm for the period 1979–2020 (Hersbach et al., 2018). Meteorological data for the study period were collected at the local weather station and included daily values of maximum and minimum air temperatures (T_{min} and T_{max}, °C), minimum and maximum relative humidity (RH_{min}, RH_{max}, %), solar radiation (R_s, MJ m^{-2} day^{-1}), wind speed measured at 2 m height (u_2, m s^{-1}), and precipitation (P, mm). A brief characterization of the weather conditions during the study period is presented in Fig. 2. In 2019, annual P totalized 336 mm and the ET_o summed 1263 mm. In 2020, annual P reached 470 mm and the ET_o summed 1248 mm.

Six years old almond trees (*Prunus amygdalus* Batsch cv. Monterey) were planted at a distance of 3.7 m within rows and 7.0 m between rows, resulting in a plant density of about 391 plants ha^{-1}, with northwest-southeast orientation. The soil was classified as Chromic Abruptic Luvisol (IUSS Working Group WRB, 2014). The soil profile was studied in two locations (hereafter denoted as P1 and P2). The main soil physical and chemical properties are given in Table 1. Particle size distribution was obtained using the pipette method (Gee and Or, 2002) for particles with a diameter of < 0.002 mm (clay) and 0.02–0.002 mm (silt), and by sieving for particles of 0.2–0.02 mm (fine sand) and 2.0–0.2 mm (coarse sand). These texture classes follow the Portuguese classification system (Gomes and Silva, 1962) and are based on the International Soil Science Society (ISSS) particle limits (Atterberg scale). Dry bulk density (ρ_b) was obtained by drying volumetric soil samples (100 cm^3) at 105°C for 48 h. Soil hydraulic properties were measured also in undisturbed 100 cm^3 soil cores. Volumetric soil water content at field capacity (θ_{FC}) was measured using suction tables at − 10 kPa matric potential (Romano et al., 2002). Volumetric soil water content at the wilting point (θ_{WP}) was measured using a pressure plate extractor at − 1500 kPa matric potential (Dane and Hopmans, 2002). The pH was measured on a suspension of soil and distilled water (1:5 soil/water) using a potentiometric method. Organic carbon (OC, %) content was determined by the Walkley–Black method (Nelson and Sommers, 1982). Exchangeable cations (Na^+, Ca^{2+}, Mg^{2+}, K^+) and the cation exchange capacity (CEC) were determined by a modified Melich method (Melich, 1948) using a solution of $BaCl_2$ +triethanolamine at pH 8.1. The electrical conductivity of the soil saturation paste extract (EC_e) was determined potentiometrically. The exchangeable sodium percentage (ESP) was determined from the ratio of exchangeable Na^+ and the CEC (U.S. Salinity Laboratory Staff, 1954).

Management practices, including irrigation and fertilization, were

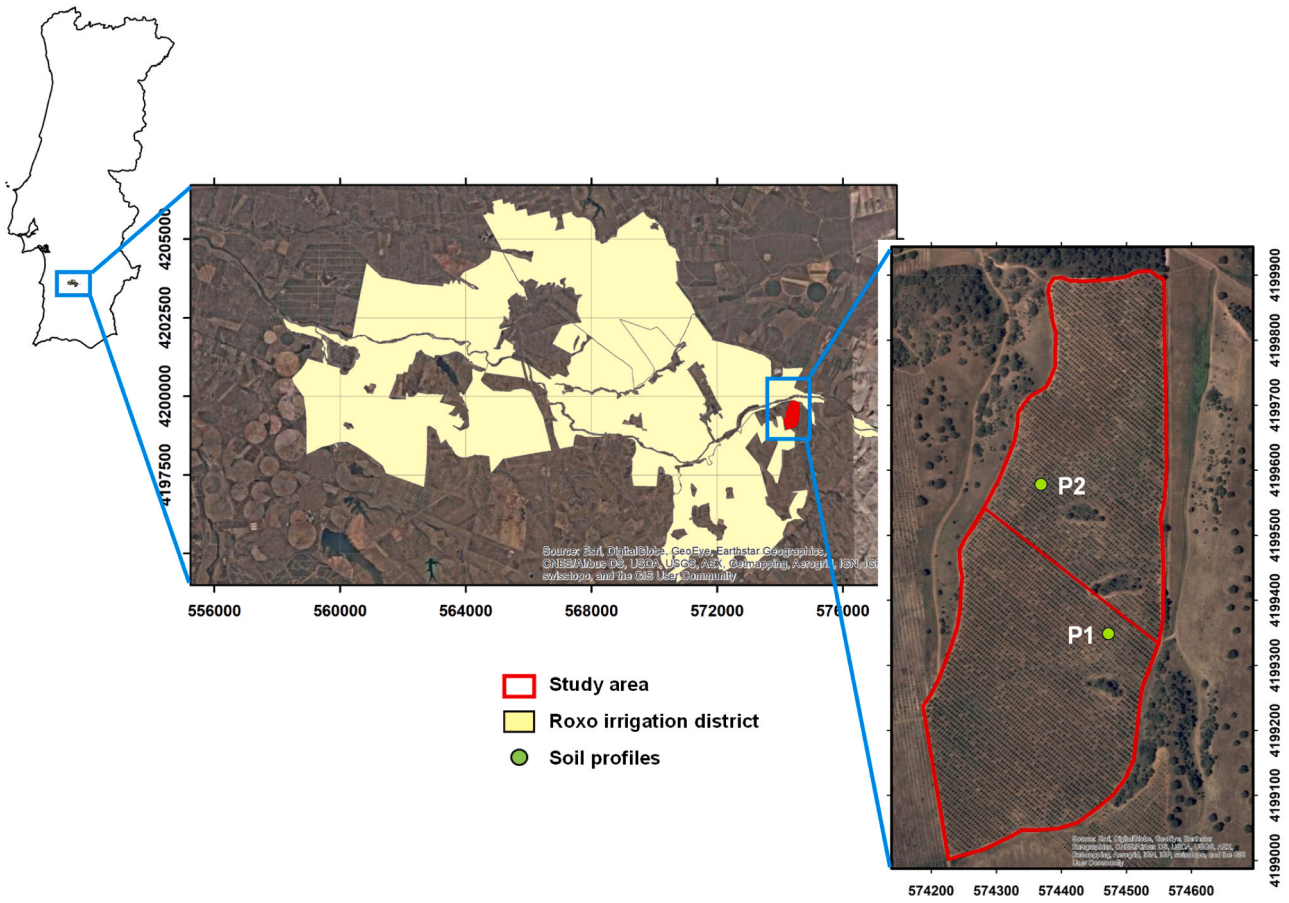

Fig. 1. Location of the study area (P1 and P2 refer to the location of the monitoring sites).

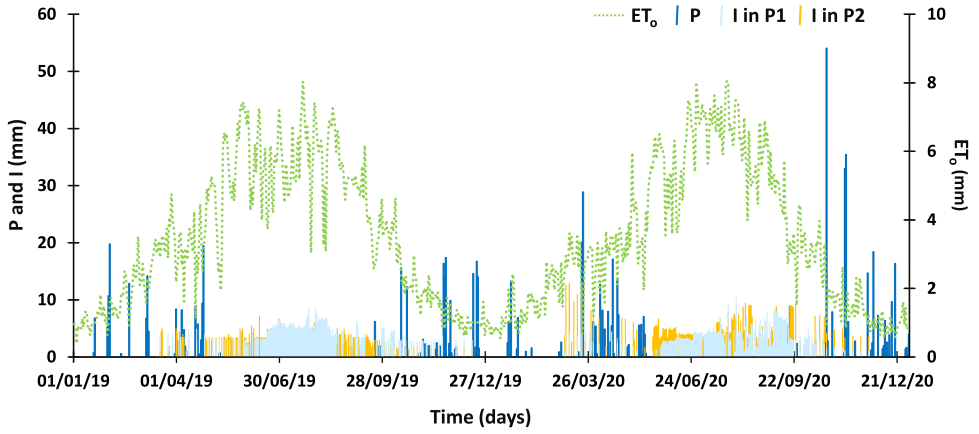

Fig. 2. Daily reference evapotranspiration (ET_o), precipitation (P), and irrigation (I) applied in monitoring sites P1 and P2 during the 2019 and 2020 growing seasons.

performed according to the standard practices in the region and were decided by the farmer. Trees were irrigated by drip irrigation, with one trickle line placed along rows and drippers spaced every 1 m. Irrigation was also monitored at P1 and P2 using flowmeters. Irrigation depths per irrigation event ranged from 1.0 to 10.5 mm at P1 and from 1.1 to 13.0 mm at P2 (Fig. 2). The average irrigation depths per irrigation event were similar (4.2–4–3 mm), but seasonal values differed between P1 and P2. Table 2 presents the monthly values of irrigation depths monitored in locations P1 and P2 during the two growing seasons. Soil water content was also continuously monitored at 0.1, 0.3, 0.5, and 0.7 m depth in both sites using EnviroPro MT capacitance probes (MAIT Industries, Australia). Probes were installed in the tree rows at approximately 0.16 m from the nearest drippers and 0.68 m from the trees. For more details on irrigation management, calibration of capacitance probes, and monitoring see Ramos et al. (2023a).

2.2. EMI survey and mapping of soil texture

The EC_a was measured in December 2019 using a DUALEM-21 (Dualem Inc., Milton, Ontario, Canada) EMI sensor. The equipment operates at a low frequency (9 kHz) and contains two horizontal coplanar (HCP) and two perpendicular (PRP) receiver arrays. The

Table 1
Physical and chemical characteristics at location 1 (P1) and 2 (P2) of the almond field.

Location	P1				P2			
Depth (m)	0.0–0.3	0.3–0.5	0.5–0.8	0.8–1.0	0.0–0.2	0.2–0.4	0.5–0.7	0.7–1.1
Texture class	SaL	CL	C	C	SaL	CL	C	L
CS (2 – 0.2 mm, %)	46.0	35.2	29.7	25.5	41.0	27.8	12.5	35.6
FS (0.2 – 0.02 mm, %)	23.7	16.6	12.4	13.8	28.0	20.0	20.5	31.8
Si (0.02 – 0.002 mm, %)	15.4	13.2	13.0	13.1	17.1	13.4	12.0	15.9
C (< 0.002 mm, %)	14.9	35.0	44.9	47.6	13.9	38.8	55.0	16.7
ρ_b (g cm^{-3})	1.33	1.41	–	–	1.48	1.41	–	–
θ_{FC} (cm^3 cm^{-3})	0.225	0.215	–	–	0.195	0.202	–	–
θ_{WP} (cm^3 cm^{-3})	0.067	0.135	–	–	0.080	0.080	–	–
pH (H_2O)	5.7	6.3	6.2	5.3	6.3	6.3	6.6	6.7
OC (g kg^{-1})	12.7	4.6	2.3	–	11.6	6.4	4.5	–
CEC (cmol$_c$ kg^{-1})	10.54	13.55	14.90	30.38	11.58	24.34	39.02	41.37
EC_e (dS m^{-1})	0.21	0.29	0.34	0.29	0.20	0.18	0.19	0.47
ESP (%)	1.44	1.34	3.03	2.70	1.19	1.83	3.42	4.84

Texture classes (SaL, sandy loam; CL, clay loam; C, clay; L, loam); CS, coarse sand; FS, fine sand; Si, Silt; C, clay; ρb, dry bulk density; θFC, soil water content at field capacity; θWP, soil water content at the wilting point; OC, organic carbon content; CEC, cation exchange capacity; ECe, electrical conductivity of the saturation paste extract; ESP, exchangeable sodium percentage.

Table 2
Crop development stages, crop coefficients (K_c), and monthly irrigation depths applied at P1 and P2 monitoring sites.

Month	Crop stage	K_c	P1 (mm)		P2 (mm)	
			2019	2020	2019	2020
Jan.	initial	0.60	0	0	0	0
Feb.	development	0.60	0	0	0	0
Mar.	mid-season	0.65	12	31	19	89
Apr.	mid-season	0.65	18	14	42	29
May	mid-season	0.65	45	15	82	68
Jun.	mid-season	0.65	109	95	122	121
Jul.	mid-season	0.65	177	123	157	139
Aug.	mid-season	0.65	124	140	110	143
Sep.	late-season	0.60	51	125	69	127
Oct.	late-season	0.60	50	47	31	37
Nov.	non-growing	0.20	22	6	13	20
Dec.	non-growing	0.20	9	0	5	0
Total	–	–	617	596	649	772

distance from the transmitter to the center of the PRP 1mPcon and 2mPcon receivers is 1.1 and 2.1 m, respectively, while the distance from the transmitter to the HCP 1mHcon and 2mHcon receivers is 1.0 and 2.0 m, respectively. When the sensor is positioned on the soil surface, the 1mPcon and 2mPcon receivers provide theoretical exploration depths of 0.0–0.5 m and 0.0–1.0 m, respectively, while the HCP 1mHcon and 2mHcon receivers provide deeper depths of exploration, 0.0–1.5 m and 0.0–3.0 m, respectively. The DUALEM-21 was mounted on a PVC sled at approximately 0.10 m above the soil surface and towed by an all-terrain vehicle. The DUALEM-21 position was measured using a real-time kinematic differential GPS receiver (Trimble, Sunnyvale, CA, USA) and an Allegro-TK6000 computer (Juniper Systems, Logan, UT, USA). To ensure accuracy, the raw georeferenced EC_a data were corrected for positional errors that may have arisen from delays in data transmission, reception, or logging during field measurement. This correction was done using the method outlined in González Jiménez et al. (2022). Subsequently, the corrected EC_a data were interpolated into a 5 × 5 m grid using the inverse distance method implemented in Surfer (Golden Software, LLC in Boulder, CO, USA), similar to other studies (e.g., Gómez Flores et al., 2022).

The EC_a data were inverted using the EM4SOIL software (Triantafilis et al., 2013a) by applying a quasi-3d (q-3d) inversion algorithm. In this software, the lateral constrained inversion algorithm developed by Monteiro Santos (2004) was used. The subsurface model is created by distributing a set of 1-D models according to the locations of the EC_a measurements. The inversion algorithm, S_2 (Sasaki, 2001), was used in this study, which is based on the Occam regularization (DeGroot-Hedlin and Constable, 1990). The forward modelling was based on the full solution (Monteiro Santos et al., 2010). The misfit function applied is determined as the square root of the sum of the squares of the differences, divided by the number of measurements and expressed in mS m^{-1}.

In addition, the algorithm requires a damping factor that regulates the smoothness of the model. As the inversion progresses, the damping factor is gradually decreased to determine more detailed model parameters. Generally, larger values produce smoother inversion results (Farzamian et al., 2019). To determine the best value for the damping factor, inversions with different damping factor values are usually performed (e.g., Zare et al., 2020). The inversion of the EC_a data was carried out by implementing an initial model with seven layers (i.e., 0.2, 0.4, 0.6, 1.0, 1.5, 3.0 m), held fixed during the inversion process. The first three layers correspond to the depth of the soil samples where real information of the real soil electrical conductivity (σ) was required for calibration, validation, and generation of soil properties from EMI data. Based on the variation of the measured EC_a at different depths, the initial model was determined with an electrical conductivity of 50 mS m^{-1} for the first two layers, 100 mS m^{-1} for 0.6 and 1 m, 200 mS m^{-1} for the deeper layers at 1.5 m, and 300 mS m^{-1} for the 3.0 m and deeper layers.

Soil was also sampled at 12 locations, at a depth of 0.0–0.2 and 0.2–0.4 m, along the DUALEM-21 survey transects. Due to the presence of rocks (coarse elements), samples could be collected to the maximum depth of 0.6 m (i.e., 0.4–0.6 m) at few locations. The locations for soil sample collection were selected after conducting the EMI survey, guided by the visual observation of the EC_a data. A total of 21 samples were collected and all samples were air-dried, crushed, passed through a 2 mm sieve, and analyzed in the laboratory for particle size distribution. The correlation between σ and particle size distribution (i.e., sand, silt, and clay fractions) was then investigated (see section 3.4).

2.3. Soil hydrological modeling

2.3.1. Model description

The MOHID-Land model (Ramos et al., 2017) was used to solve the equation for the soil water balance in a grid defined over the case study area:

$$ET_a + RO + DP - I - P - \Delta S = 0 \quad (1)$$

where ΔS is the change in soil water storage (mm), ET_a is the actual evapotranspiration (mm), RO is the surface runoff (mm), DP is the deep percolation (mm), I is the irrigation depth (mm), and P is the precipitation amount (mm), all computed between time steps, and summed for the intended analysis for the total length of each growing season. As a fully distributed model, MOHID-Land organizes the simulation domain in a regular structured grid, quadrangular or rectangular in the

horizontal plane, and cartesian in the vertical plane. The model then considers the interactions between cells in the vertical or lateral direction, formulating the fundamental processes at a fine spatial (cells) and temporal scale, contributing to the overall dynamics at a higher level of organization such as the field scale. A finite-volume approach is adopted.

The atmosphere provides the necessary data for the imposition of surface boundary conditions that may be spatially and temporally variable. In this study, these were daily irrigation and precipitation depths as well as crop evapotranspiration rates (ET_c, L T^{-1}). Irrigation and rainfall depths were user defined. The ET_c was obtained from the product of the single crop coefficient (K_c) and the reference evapotranspiration (ET_o, L T^{-1}) computed by the FAO PM equation (Allen et al., 1998). ET_c values were then partitioned into potential soil evaporation (E_p, L T^{-1}) and crop transpiration (T_p, L T^{-1}) as a function of simulated leaf area index (LAI, m^2 m^{-2}) following Ritchie (1972). The LAI, as well as other crop growth state variables (total biomass, root depth, crop height) were simulated using a modified version of the EPIC model (Williams et al., 1989; Neitsch et al., 2011). This model is based on the heat unit theory, which assumes that all heat above the base temperature accelerates crop growth and development. The main factors affecting the development of LAI, the most relevant crop state variable for this application, are the cumulative heat units during the crop season, crop stage, and crop stress (temperature and water) (Neitsch et al., 2011).

Infiltration and surface runoff were partitioned from rainfall and irrigation data using a Darcian based approach. The variable saturated flow in the porous medium was then computed using Richards equation as follows:

$$\frac{\partial \theta}{\partial t} = \frac{\partial}{\partial D_i}\left(K(\theta)\left(\frac{\partial h}{\partial D_i} + \frac{\partial}{\partial D_i}\right)\right) - S(h) \quad (2)$$

where θ is the volumetric water content (L^3 L^{-3}), t is time (T), D is the distance between two points (L), i represents the xzy directions (-), h is the soil pressure head (L), K is the hydraulic conductivity (L T^{-1}), and S is a sink term accounting for water uptake by plant roots (L^3 L^{-3} T^{-1}). The unsaturated soil hydraulic properties were described using the Mualem-van Genuchten (MvG) functional relationships (Mualem, 1976; van Genuchten, 1980):

$$S_e(h) = \frac{\theta(h) - \theta_r}{\theta_s - \theta_r} = \frac{1}{(1 + |\alpha h|^{\eta})^m} \quad (3)$$

$$K(h) = K_s S_e^{\lambda}\left[1 - \left(1 - S_e^{1/m}\right)^m\right]^2 \quad (4)$$

where S_e is the effective saturation (-), θ_r and θ_s denote the residual and saturated water contents (L^3 L^{-3}), respectively, K_s is the saturated hydraulic conductivity (L T^{-1}), α (L^{-1}) and η (-) are empirical shape parameters, $m = 1–1/\eta$, and λ is a pore connectivity/tortuosity parameter (-). The Richards equation was used in the whole subsurface domain and simulates saturated and unsaturated flow using the same grid that defines the porous medium.

The sink term (S) in the Richards equation was computed following the macroscopic approach proposed by Feddes et al. (1978). In this approach, potential transpiration (T_p, L T^{-1}) is linearly distributed over the root zone, resulting in the function $T_p(z)$, which is diminished as a function of soil pressure head (Skaggs et al., 2006; Šimůnek and Hopmans, 2009). The piecewise linear model proposed by Feddes et al. (1978) was adopted for computing actual transpiration rates (T_a, L T^{-1}). In this approach, the water uptake is assumed to be equal to the potential rate when the pressure head is between h_2 and h_3, drops off linearly when $h > h_2$ or $h < h_3$, and becomes zero when $h < h_4$ or $h > h_1$ (subscripts 1–4 denote for different threshold pressure heads). Actual soil evaporation (E_a, L T^{-1}) was obtained by limiting E_p values using a threshold pressure head (American Society of Civil Engineers ASCE, 1996).

Finally, surface runoff or overland flow, which results from the amount of water that does not infiltrate into the soil, was simulated at the surface of the porous medium domain by solving a Saint-Venant equation in its conservative form that accounts for advection, pressure, and frictional forces for two horizontal directions (Trancoso et al., 2009).

2.3.2. Model setup

The MOHID-Land model was implemented in the study area (22.6 ha) using a 5 m square horizontal grid. This resolution was chosen to better incorporate the detailed information from the EMI survey. The digital terrain model (DTM) was obtained from the interpolation of elevation data collected during the field soil survey using inverse distance weighting (Fig. 3). The vertical grid was discretized into nine layers, ranging in thickness from 0.1 m at the surface to 0.5 m at the soil bottom. A coarse discretization of the soil domain was necessary to maintain the computational time within reasonable limits. Each grid column was also divided into three soil horizons (by grouping the layers of the vertical grid) to best match the soil layers in the EMI data. The first horizon was defined from the soil surface to 0.2 m depth, included the two top layers of the vertical grid, and corresponded to the information provided by the EMI sensor at 0.2 m. The second horizon was defined from 0.2 to 0.4 m depth, also included two grid layers, and was made to correspond to the EMI data at 0.4 m. The third soil horizon was defined from 0.4 m to soil bottom (2.5 m), included five grid layers, and incorporated the information provided by the EMI sensor at 0.6 m depth.

The MvG soil hydraulic parameters (θ_r, θ_r, α, η, K_s) were estimated for each cell of the simulation domain from the soil particle size distribution maps produced from EMI data using the pedotransfer functions (PTFs) listed in Table 3. The pore connectivity/tortuosity λ parameter was simply set to 0.5 following Mualem (1976). The adopted PTFs were developed using the content of the PROPSOLO database (Gonçalves et al., 2011; Ramos et al., 2013, 2014a), which includes data on soil basic and hydraulic properties of 697 horizons/layers of 330 soil profiles studied in Portugal. The PTFs were established using multiple regression analysis, with the equations for each MvG parameter determined individually using particle size distribution and the average depth of the soil layer as inputs. This was done to match the available information provided by the soil texture maps. For each equation, the dataset was split into a calibration set comprising 75% of the data, and a validation set with the remaining 25%. The random split and subsequent model development and validation were performed 10 times. Each time, the data that were used in the development of the PTFs was not used in validation, and vice versa. The PTFs were then established by averaging the regression coefficients of each argument obtained for each of the 10 randomly generated datasets (Ramos et al., 2013, 2014b).

The multiplying factor (f_h) to obtain the horizontal saturated hydraulic conductivity from K_s ($f_h = K_{s\ horizontal}/K_{s\ vertical}$) was set to a value of 10 following Oliveira et al. (2020). For the initial conditions, the soil water content was set to the field capacity. The bottom and lateral boundaries of the grid domain were left open for free drainage. The development of the crop was simulated using the default vegetation growth parameters for orchards in Neitsch et al. (2011). The root depth was assumed to follow a linear distribution up to a maximum depth of 1.0 m. The Manning coefficient (0.043 s $m^{-1/3}$) was adapted from van der Sande et al. (2003). The precipitation and the FAO56 ET_o data (Allen et al., 1998) presented in Fig. 2 were used. The FAO56 ET_o data were combined with a K_c value to compute the daily ET_c value. The K_c values for the initial, mid, and end season stages were defined according to Rallo et al. (2021), while a value of 0.2 was assumed for the non-growing period (Table 2). K_c values were updated only monthly considering the different crop stages of a growing season. Irrigation data were obtained from field monitoring and expressed as daily values (Fig. 2). It was assumed that P1 data represented irrigation in the southern part of the field, while P2 data described irrigation in the northern side (Fig. 1). The

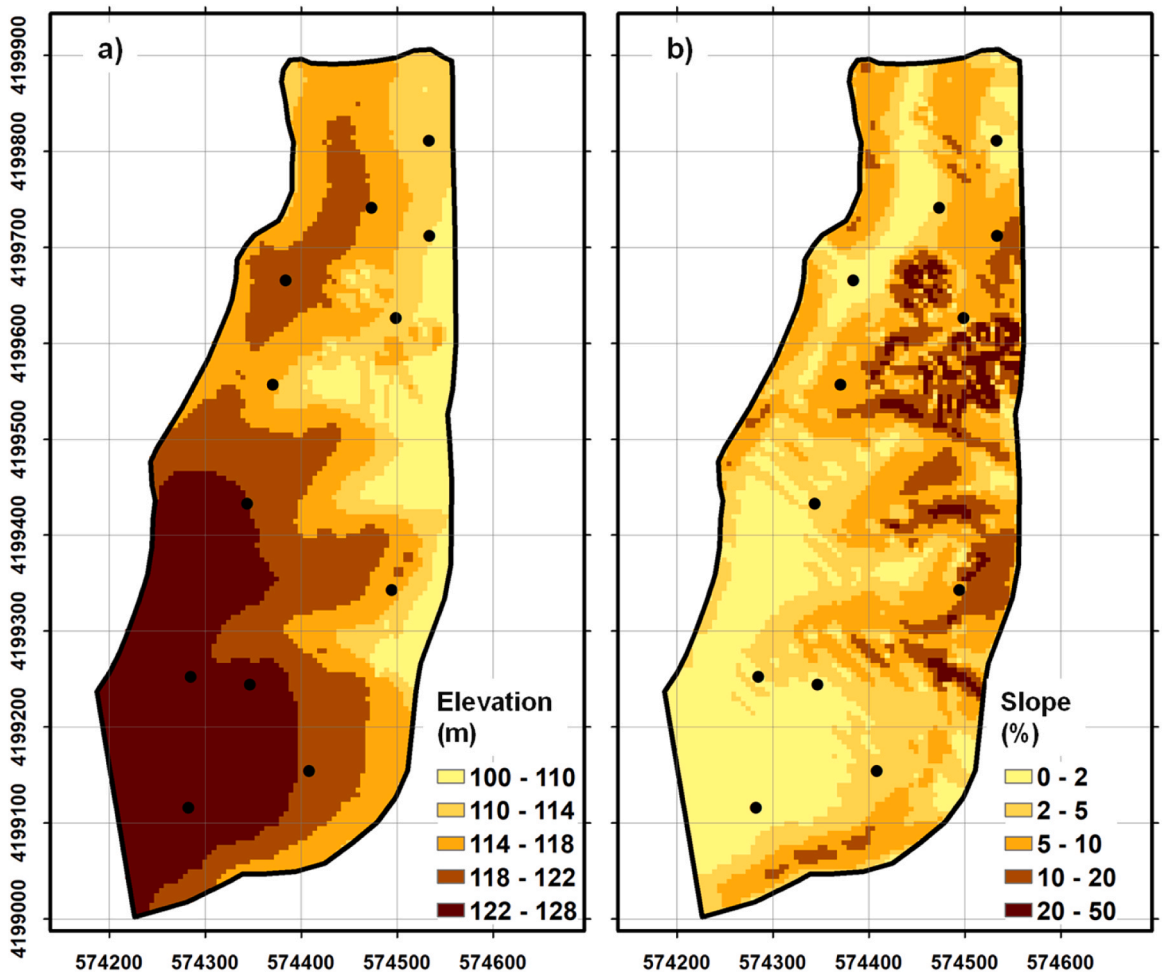

Fig. 3. Digital terrain model of the study area: elevation (a), and slope (b).

Table 3
Pedotransfer functions used in this study.

Parameter	Equation
θ_r ($m^3\ m^{-3}$)	*0.025 + 0.002 Clay*
θ_s ($m^3\ m^{-3}$)	*0.556 – 0.002 Sand – 0.000253 Z*
log (α) (-)	*–1.164 – 0.018 Silt + 0.01 Clay – 0.001 Z*
η	*1.417 – 0.006 Clay + 0.001 Z – 0.002 Silt*
log (K_s) (-)	*2.329 – 0.011 Silt*

Note: θ_r, residual water content; θ_s, saturated water content; α and η, empirical shape parameters; K_s, saturated hydraulic conductivity; Z, mean soil layer depth. Sand (coarse sand + fine sand), Silt, and Clay are defined according to the International Soil Science Society particle limits.

northern (10.3 ha) and southern (12.3 ha) sides were thus assumed to represent two distinct irrigation blocks of the same almond field. The soil pressure heads for computing T_p reductions due to water stress were adapted from Phogat et al. (2018), with h_1= −0.10 m, h_2= −0.25 m, h_3= −8.0 m, and h_4= −150 m.

2.4. Calibration and validation procedures

The combined use of EMI sensing and distributed three-dimensional hydrological modelling proposed in this study was evaluated in three ways: (i) the relationship between σ and particle size distribution; (ii) the capability of the hydrological model in simulating soil water contents at different depths, specifically at locations P1 and P2, and estimating the soil water balance at the field scale; and (iii) the relationship between model estimates of T_a and biomass and the Normalized Difference Vegetation Index (NDVI; Rouse et al., 1973).

Firstly, the correlation between σ and particle size distribution (i.e., sand, silt, and clay fractions) was investigated. Subsequently, calibration equations were developed using a linear regression (LR) between σ and the soil properties that exhibited significant correlation. To assess the prediction ability of the calibrations, a cross-validation procedure was conducted utilizing the leave-one-out method (LOOCV). In LOOCV, one soil sample at a specific depth was removed, and a calibration was established based on the remaining samples to predict the desired soil property at the removed sampling point. This iterative process was repeated for each of the 21 soil sampling points (from the 12 sampling sites) being removed once.

The prediction ability of the calibrations was evaluated using the root mean square error (RMSE), the mean error (ME), and Lin's concordance (CCC), respectively given as (Legates and McCabe, 1999; Lin, 1989):

$$RMSE = \sqrt{\frac{\sum_{j=1}^{n}(O_j - P_j)^2}{n-1}} \quad (5)$$

$$ME = \frac{1}{n}\sum_{j=1}^{n}(O_j - P_j \quad) \quad (6)$$

$$CCC = \frac{2S_{OP}}{S_O^2 + S_P^2 + (\overline{O} - \overline{P})^2} \quad (7)$$

where O_i and P_i are the observed and predicted soil property at location j, respectively, n is the number of observations, $\overline{O}$ and $\overline{P}$ are the means for the observed and predicted soil property, respectively, S_O^2 and S_P^2 are the corresponding variances, and S_{OP} is the covariance between the two, which is computed as follows:

$$S_{OP} = \frac{1}{n}\sum_{j=1}^{n}\left(O_j - \overline{O}\right)\left(P_j - \overline{P}\right) \quad (8)$$

RMSE represents the square root of the mean of the squared differences between the measured and predicted soil properties, indicating the concentration of data around the LR. A smaller RMSE suggests higher precision in the prediction. ME calculates the mean of all differences between the measured and predicted soil properties and assesses whether the LR consistently over- or underestimates the predicted values. A ME closer to zero implies less bias in the prediction. Lin's concordance measures the agreement between the measured and predicted values and ranges from − 1–1, with perfect agreement at 1 (Lin, 1989). A higher Lin's concordance indicates a closer alignment of the LR to the 1:1 relationship, signifying better agreement between measured and predicted values. McBride (2005) suggests that the prediction agreement can be categorized according to the Lin's whereby it is excellent (> 0.9), strong (0.8 – 0.9), moderate (0.65 – 0.8), and poor (< 0.65).

Regarding the hydrological modeling, the MOHID-Land model simulations were run from January 1st, 2018 to December 31st, 2020. The first year was used as a "warm-up" period for the model and the results were not included in the analysis. This was done to assure that initial conditions would not affect estimates of the soil water balance computed with the MOHID-Land model. The variability of the components of the soil water balance was then assessed on annual basis considering the length of the almond growing season. The following seasonal maps were calculated at the field scale:

- Infiltrated water (mm);
- Potential (T_p, mm) and actual (T_a, mm) crop transpiration, and respective T_a/T_p ratio;
- Potential (E_p, mm) and actual (E_a, mm) soil evaporation, and respective E_a/E_p ratio;
- Deep percolation (DP, mm) computed from fluxes at 1.5 m depth;
- Surface runoff (RO, mm);
- Mean soil water storage in the 0.0 − 1.5 m layer (θ_{mean}, mm), computed by averaging simulated daily soil water storage values (i.e., the sum of the product of soil water contents in different soil layers and respective layer thicknesses);
- Relative soil water storage in the 0.0 − 1.5 m layer (θ_{rel}), computed as the fraction between θ_{mean} and maximum soil water storage (i.e., the sum of the product of soil water contents at saturation in different soil layers and respective layer thicknesses);
- Variance of daily soil water storage ($\theta_{variance}$, mm^2) in the 0.0 − 1.5 m layer, computed as the variance of simulated daily soil water storage values.

This hydrological modelling application did not include a standard calibration/validation as the primary objective was only to test the use of EMI data as a proxy for soil properties variability. Nevertheless, the performance of the MOHID-Land model was assessed by directly comparing model simulations of soil water content with the dataset measured at P1 and P2 at the 0.0–0.2, 0.2–0.4, and 0.4–0.6 m soil layers during 2019 and 2020. The goodness-of-fit indicator used for this comparison was the RMSE (Eq. 5). The main difference from Eq. 5 was that, for this assessment, O_j and P_j are the observed and predicted soil water contents at time j, respectively.

Lastly, model estimates of T_a and biomass were correlated with the NDVI (Rouse et al., 1973), computed from Sentinel-2 red and infra-red bands (10 m resolution) acquired from the Copernicus Open Access Hub (Copernicus, 2023) from March to August of the 2019 and 2020 growing seasons. The Pearson correlation coefficient was used in the analysis, and no downscaling of the NDVI images to the resolution of the model domain (5 m) was done.

3. Results and discussion

3.1. Spatial distribution of soil electrical conductivity and soil properties

Fig. 4 shows the spatial distribution of the real soil electrical conductivity (σ) at the depths of 0.0–0.2, 0.2–0.4, and 0.4–0.6 m, after the inversion of the EC_a data. In the surface layer (0.0–0.2 m), σ was generally less than 50 mS m^{-1}, except near the eastern boundary of the field where σ was greater than 50 mS m^{-1}. This area corresponded to the lowest elevations. The σ values increased significantly in depth, reaching up to 180 mS m^{-1} at 0.4–0.6 m depth in the eastern and north-eastern parts of the field. The southern zone, in contrast, showed lower σ values and less variation with depth. More samples were taken in the northern part of the field due to the greater variability of EC_a (Fig. 4).

Fig. 5a and b show the LR between the clay content and σ and between the sand content and σ for all the sampling points, respectively. The figure shows that site-specific LR to predict clay and sand content could be developed with coefficients of determination (R^2) of 0.73 and 0.71, respectively, according to the following equations:

$$clay\ (\%) = 0{\cdot}193\ \sigma + 14{\cdot}67 \quad (9)$$

$$sand\ (\%) = -0{\cdot}162\ \sigma + 66{\cdot}32 \quad (10)$$

No good correlation was found between silt content and σ. Fig. 5c and d show the results of the LOOCV of the developed LR described above. In the case of clay content estimation, the ME was − 0.03% and the RMSE was 5.68%, which indicates a satisfactory prediction ability given the large range of clay content (11–52%). The CCC of 0.85 showed a strong accord between the measured and predicted clay content. For sand prediction and given the large range of sand content (31–74%), the statistical results were similar to those obtained for clay, with a slightly lower RMSE of 5.05% and a lower ME of − 1.31% compared to clay. ME values indicate that, for both clay and sand predictions, the developed LR slightly underestimated them; however, with clay, the ME values were so small as to be almost zero. The CCC for sand estimation was also slightly lower at 0.82, yet it still indicates a good accord between the measured and predicted sand content, according to McBride (2005). Since silt and σ did not correlate, silt content was calculated by closing the mass balance between sand, clay, and silt. The resulting maps showed sand contents ranging from 50.5% to 64.5% and from 26.8% to 63.2% in the 0.0–0.2-m and 0.4–0.6-m layers, respectively. The clay content ranged from 17.0% to 33.5% and from 18.4.9% to 61.4% in the layers of 0.0–0.2-m and 0.4–0.6-m, respectively (Fig. S1 and S2 in the supplementary material).

Fig. 6 presents maps of the MvG soil hydraulic parameters obtained after applying the regional PTFs from Table 3. The EMI-derived texture maps presented in Fig. S2 were used as input, along with the inclusion of the silt map (not shown), which was obtained by closing the mass balance. The additional input was the mean depth of each soil layer (Z). Histograms showing the relative frequency of values for each parameter are given in Fig. S3. As expected, higher θ_s and lower α and η corresponded to higher clay content. Lower θ_s and higher α and η corresponded to higher sand contents. Higher K_s values were also observed in areas with higher clay content, but the range of variation for this parameter was quite reduced (133–158 cm d^{-1}). These maps, which further include the map with the distribution of θ_r, were then used as input to the MOHID-Land model for the computation of the soil water balance during the 2019 and 2020 growing seasons.

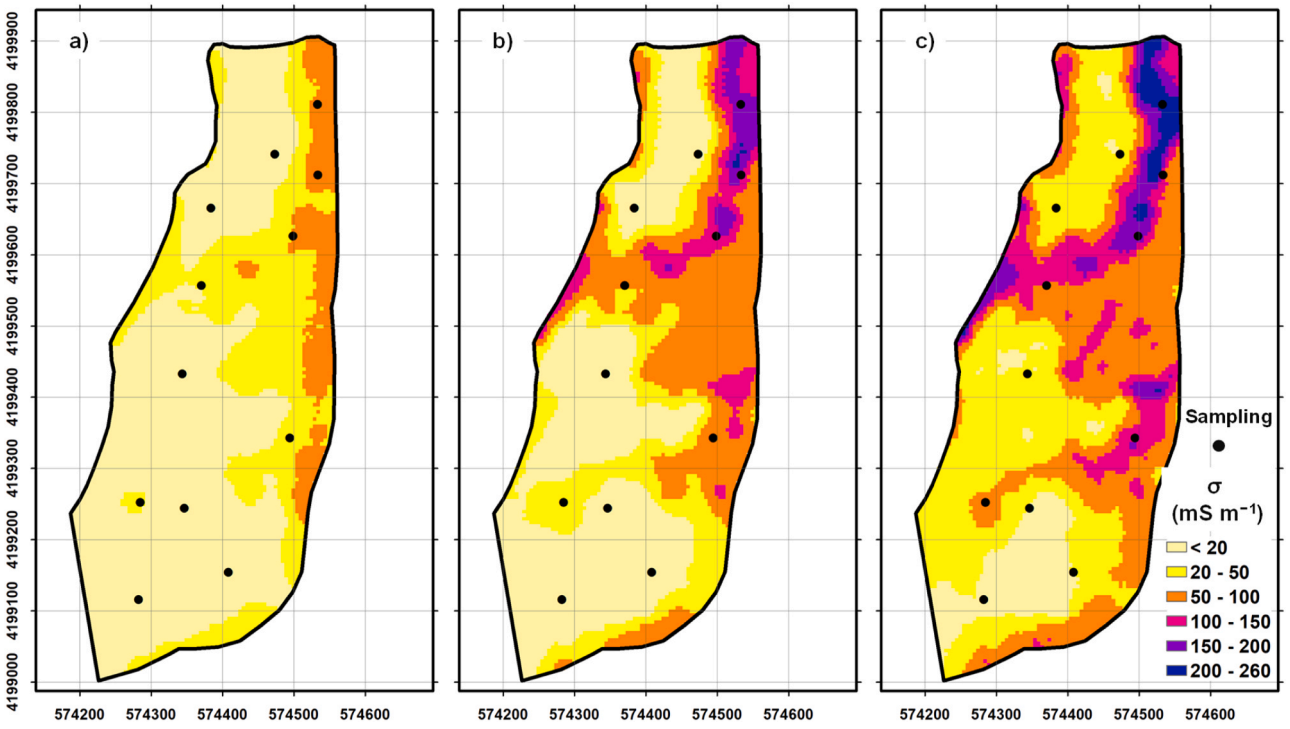

Fig. 4. Maps of the real soil electrical conductivity (σ) surveyed at 0–0.2 m (a), 0.2–0.4 m (b), and 0.4–0.6 m (c) depths and soil sampling locations.

3.2. Variability of the soil water balance at the field scale

Fig. 7 shows the spatial distribution of seasonal beneficial (actual transpiration, T_a) and non-beneficial (actual soil evaporation, E_a) water use on the almond field during the 2019 growing season. The T_a and E_a ratios in relation to their potential values are also represented. The results for 2020 were similar to those for 2019 and are therefore not shown. The seasonal T_a values summed up to about 340 mm in most of the field in both seasons. Seasonal E_a values ranged roughly from 183 to 212 mm, with a small difference between the northern and southern parts of the field because of the different irrigation depths in P1 and P2.

In most of the field, the crop was never affected by water stress, i.e., the seasonal T_a values corresponded to the T_p values. However, in areas with steeper slopes and lower elevations in the eastern and north-eastern part and in the northern half of the field, the seasonal T_a values were lower than the potential T_p values. Water stress in slope areas corresponded to water deficits as a result of surface or subsurface water flow. Water stress in low elevation areas corresponded to the locations where water accumulated, leading to apparent waterlogged conditions. As consequence, E_a was higher in these areas, and E_p values (620–630 mm) were often reached.

Fig. 8 shows the spatial distribution of infiltration, runoff, and deep percolation in the almond field. Although trends were similar, the results are presented for both seasons as the wetter conditions in 2020 help to clarify the infiltration process and the appearance of surface and subsurface water patches. Total annual infiltration of rainfall and irrigation water was relatively homogeneous in most part of the field and ranged from 954 to 986 mm and from 1080 to 1255 mm in 2019 and 2020, respectively. In 2020, the greater difference in infiltration between the northern and southern part of the field compared to 2019 was mainly due to larger difference in irrigation depths measured in P1 and P2 (Table 2). As a result of the distributed three-dimensional modelling approach, which accounts for vertical and lateral interactions between cells in the simulated domain, water that did not infiltrate in one cell of the surface domain generated surface runoff (*RO*) and eventually increased infiltration in the adjacent downslope cells. This was observed in the *RO* estimates, which were only relevant in slope areas where the annual total *RO* summed 364–377 mm at certain locations. In the lower parts of the field, the accumulation of water resulted in greater total infiltration than that possible by the sum of seasonal precipitation and rainfall values. Deep percolation (*DP*) from the root zone layer was also consistent with these results. In most of the field, *DP* was similar, ranging from 413 to 426 mm and from 522 to 645 mm in 2019 and 2020, respectively. *DP* was higher in the depressed areas (>800 mm), although infiltration was lower at some of these sites (i.e., the rate of water percolation exceeded that of water infiltration in these locations). This shows that subsurface runoff processes played an important role in the soil water dynamics simulated in this modeling application.

Finally, Fig. 9 presents the spatial variability of mean (θ_{mean}) and relative (θ_{rel}) soil water storage in 2019 and 2020. Also depicted are the spatial distribution variances in soil water content (θ_{var}) in both seasons. The maps of θ_{mean} show clear agreement with other modeling results, i.e., higher values in areas where water tends to accumulate and where the values of E_a and *DP* were higher. However, as θ_{mean} is strongly dependent on the soil hydraulic properties, θ_{rel} may be a more appropriate variable for assessing the trends associated with water storage in the soil. Nevertheless, the same observations can be made. The distribution of θ_{rel} show that the values in the lower areas are closer to saturation, where water tends to accumulate, and then evaporate, or percolate. This was confirmed by θ_{var}. The low variance values were found at the same locations because there was small variation in soil water storage since the soil was kept largely saturated throughout the simulation periods.

It is important to note that the apparent waterlogged conditions described above were artificially and unintentionally created through the implementation and parameterization of the model in the study field. However, these areas do refer to locations where crop growth was less favorable as observed in the field. Specifically, these areas correspond to field depressions, where the clay content is higher, particularly at a depth of 0.4–0.6 m. As a consequence of the higher clay content, the soil hydraulic properties in these areas correspond to increased soil water storage capacity. Furthermore, the use of a coarse discretization in the soil domain, which was necessary for three-dimensional modeling at the field scale to ensure reasonable computational efficiency, had a

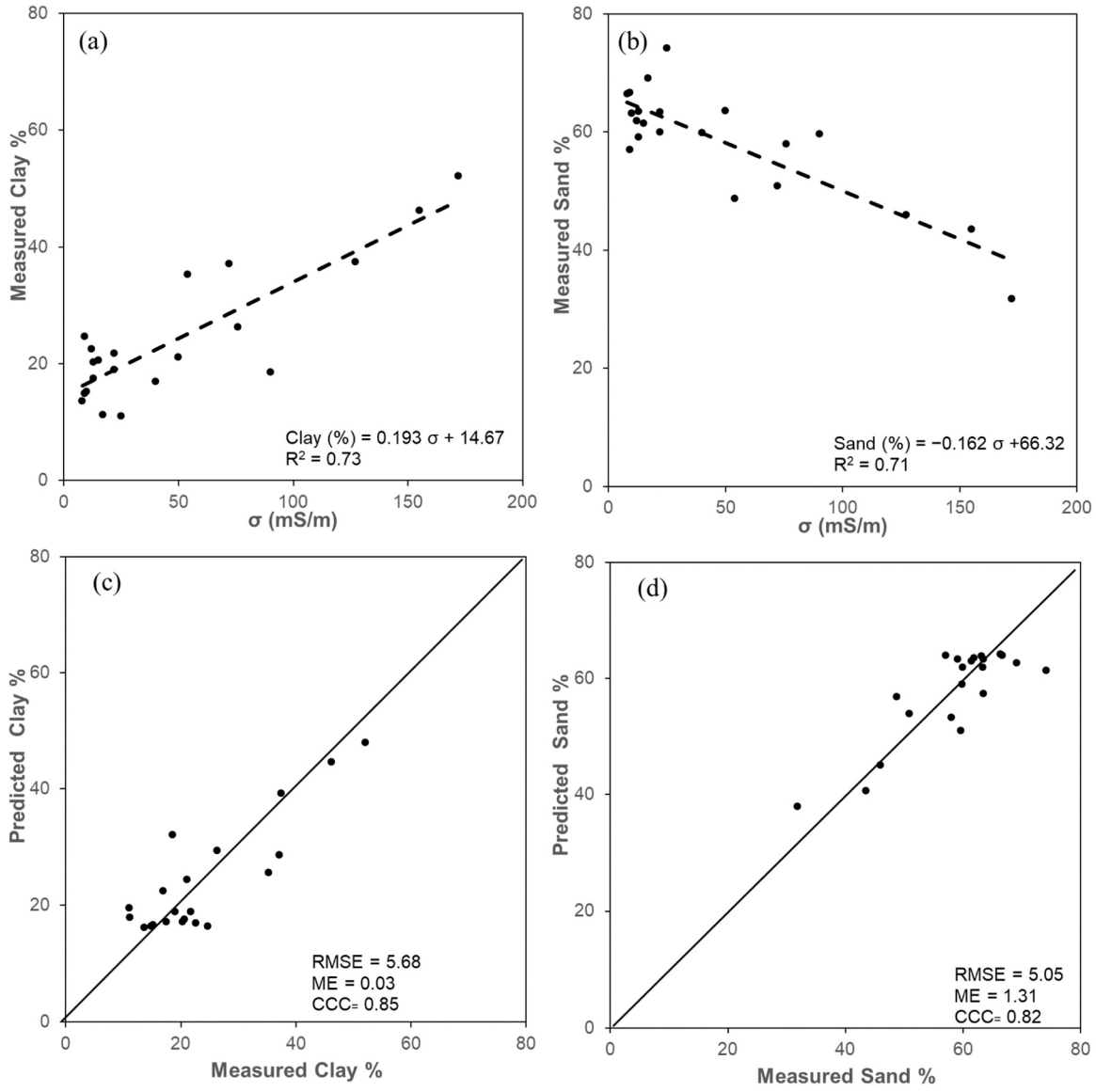

Fig. 5. Scatterplots of (a,c) the soil electrical conductivity (σ, mS m^{-1}) and the measured clay and sand contents (%) (the dashed line corresponds to the linear regression (LR) of the calibration equation), and (b,d) validation results of the LR calibration equation calculated for clay and sand contents using LOOCV method.

notable impact on the infiltration process, as it reduced hydraulic gradients and fluxes between grid cells. As a result, not only were grid cells capable of storing more water, but fluxes between cells were also diminished. Another factor contributing to the accumulation of water in the depressed areas was the simplified approach used in MOHID-Land to represent soil anisotropy. By relating horizontal and vertical soil hydraulic conductivities with a multiplying factor (f_h) of 10, subsurface flow was partially promoted towards the depressed areas.

3.3. Validation and development needs

Inversion of the interpolated EC_a data provided high-resolution maps of σ across the almond field. Simple linear relationships were then established between σ and clay and σ and sand, using a relatively small number of samples. Soil texture and σ were thus highly collinear. High σ values corresponded to high clay and low sand contents. Other approaches such as neural networks have been proposed to reduce this collinearity dependence and better distinguish the relationships between σ and soil texture from the confounding effects of other soil properties that influence σ, such as soil salinity, pH, and CEC (e.g., Cockx et al., 2009; Kelley et al., 2017). However, such approaches would require more field data than that available in this study.

The DUALEM-21 sensor has relatively low sensitivity to variations in topsoil conductivity (< 0.5 m), in accordance with its sensitivity function and theoretical depth of investigation. Moreover, a smoothness constraint was imposed in the modelling to stabilize the inversion and smooth conductivity variations over short depth increments (e.g., Farzamian et al., 2021). To improve the prediction of topsoil texture, other EMI multi-coil sensors such as DUALEM-1S or CMD Mini Explorer 6 L can be used. These sensors are designed for detailed investigation of the topsoil as they have multiple receivers at a short distance from the transmitter, thus providing more detailed EC_a data for the topsoil. In the absence of such a sensor, multi-height EC_a measurements (e.g., Farzamian et al., 2023) might also help to better resolve topsoil conductivity variations in short depth increments.

Soil hydraulic properties maps were produced from soil texture maps using regional PTFs (Table 3). The relationships between σ and soil hydraulic data were also highly collinear, while other issues arise when using PTFs. It is well known that PTFs using particle size distribution data as the only input perform poorly. Information on soil structure is

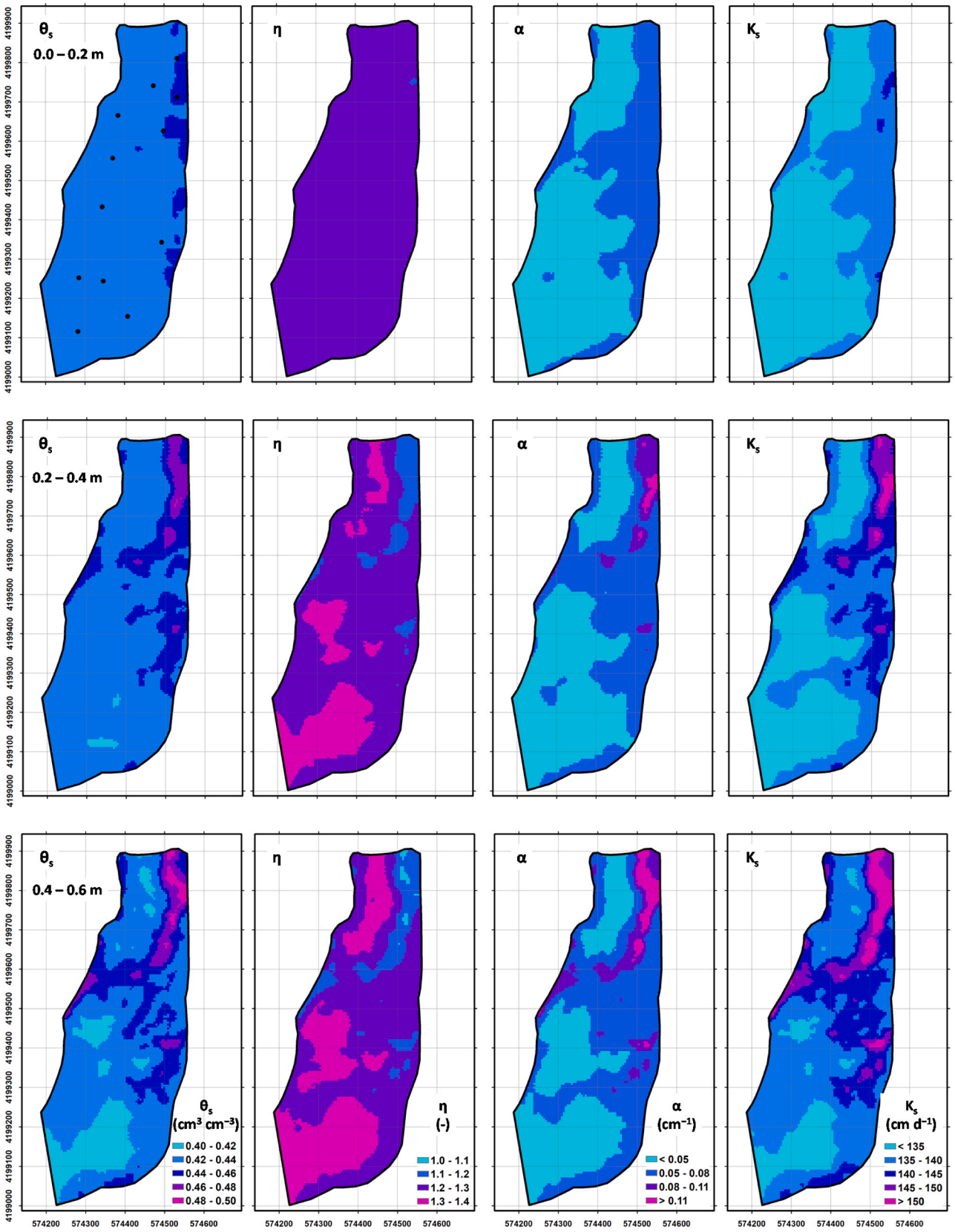

Fig. 6. Spatial distribution of the MvG soil hydraulic parameters at 0.0–0.2 m (top), 0.2–0.4 m (middle), and 0.4–0.6 m (bottom) depths (θ_s, saturated water content; α and η, empirical shape parameters; K_s, saturated hydraulic conductivity).

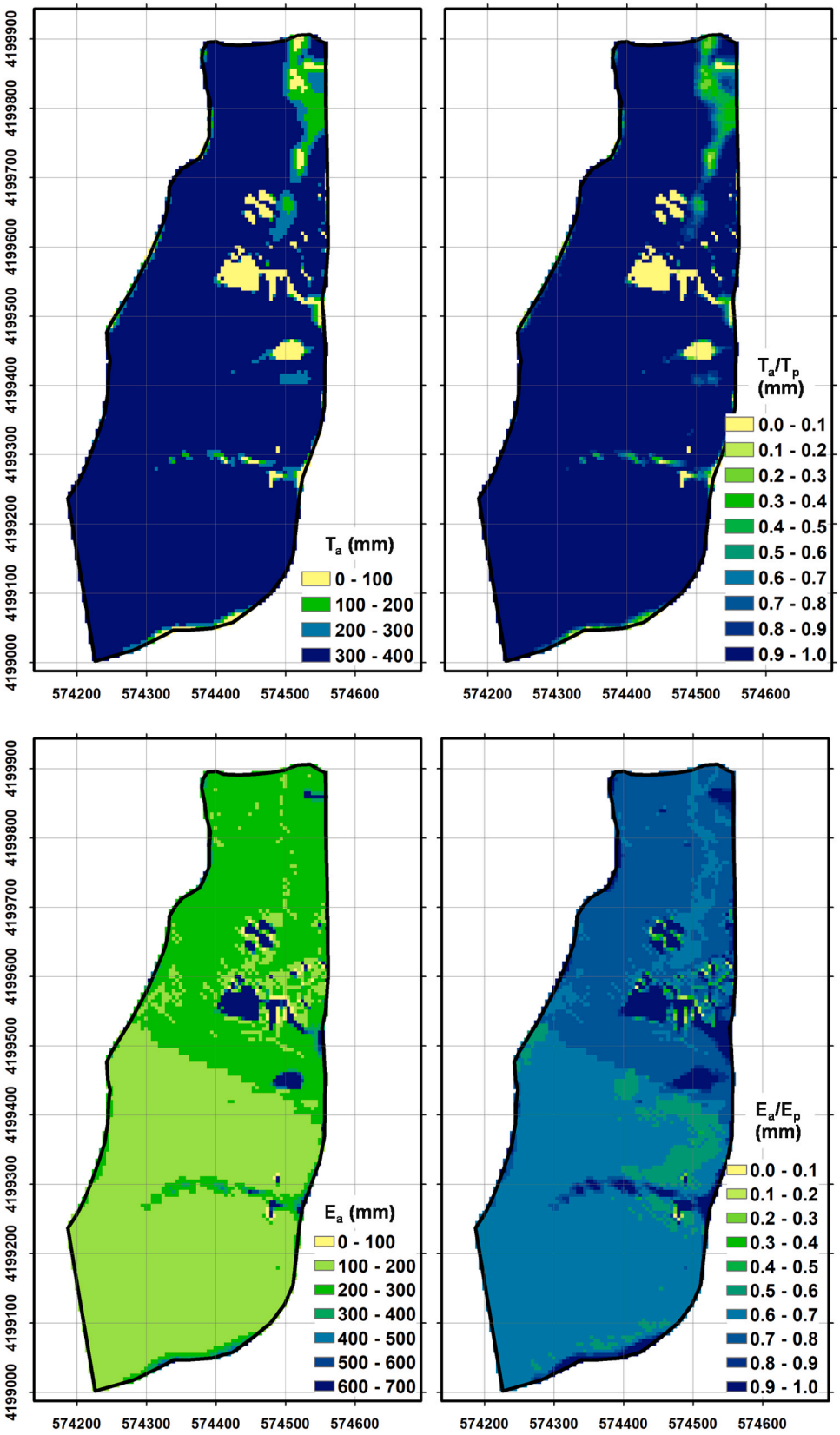

Fig. 7. Spatial distribution of actual transpiration (T_a), actual soil evaporation (E_a), and T_a/T_p and E_a/E_p ratios in 2019. Similar maps were observed for 2020 (not shown).

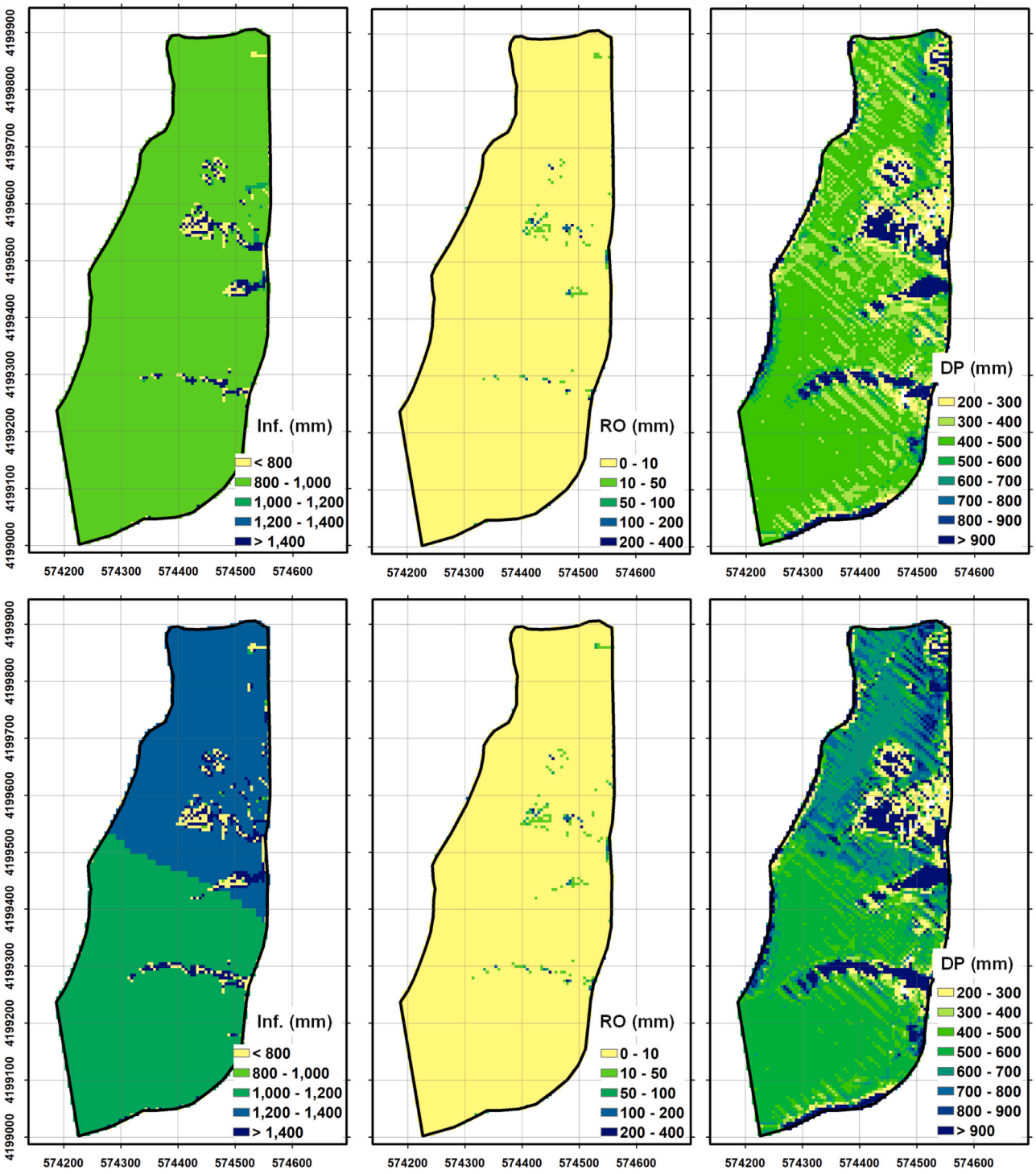

Fig. 8. Spatial distribution of infiltration (Inf.), surface runoff (*RO*) and deep percolation (*DP*) in 2019 (top) and 2020 (bottom).

equally important to reduce the unexplained variability in soil hydraulic data (Weihermüller et al., 2021; Van Looy et al., 2017; Wösten et al., 2001). However, soil structure can hardly be assessed with EMI. Also, using the total sand content (2.0 – 0.02 mm) instead of the corresponding partitioned fractions, namely coarse (2.0 – 0.2 mm) and fine sand (0.2 – 0.02 mm), as commonly employed in inferring particle size limits of the Atterberg scale, has resulted in further increased model errors. As shown in Ramos et al. (2023c), this results in RMSE values ranging from 0.057 to 0.097 cm^3 cm^{-3} for estimates of soil water retention data at different matric heads and 0.860 for log (K_s), which are generally worse than when adopting PTFs that use coarse and fine sand fractions as arguments (RMSE of 0.038–0.055 cm^3 cm^{-3} for soil water retention data and 0.588 for log(K_s)). More specific relationships between σ and the granulometric fractions than those established in Eqs. (9) and (10) are therefore needed to reduce model errors. Considering the further partitioning of the coarse and fine sand components into smaller fractions would likely be helpful in improving the accuracy of estimates. This can be achieved using data already stored in the PROPSOLO soil database (Gonçalves et al., 2011), and seems preferable to using external PTFs since estimates from regional PTFs usually outperform the former at the field scale (Horta et al., 2023; Van Looy et al., 2017).

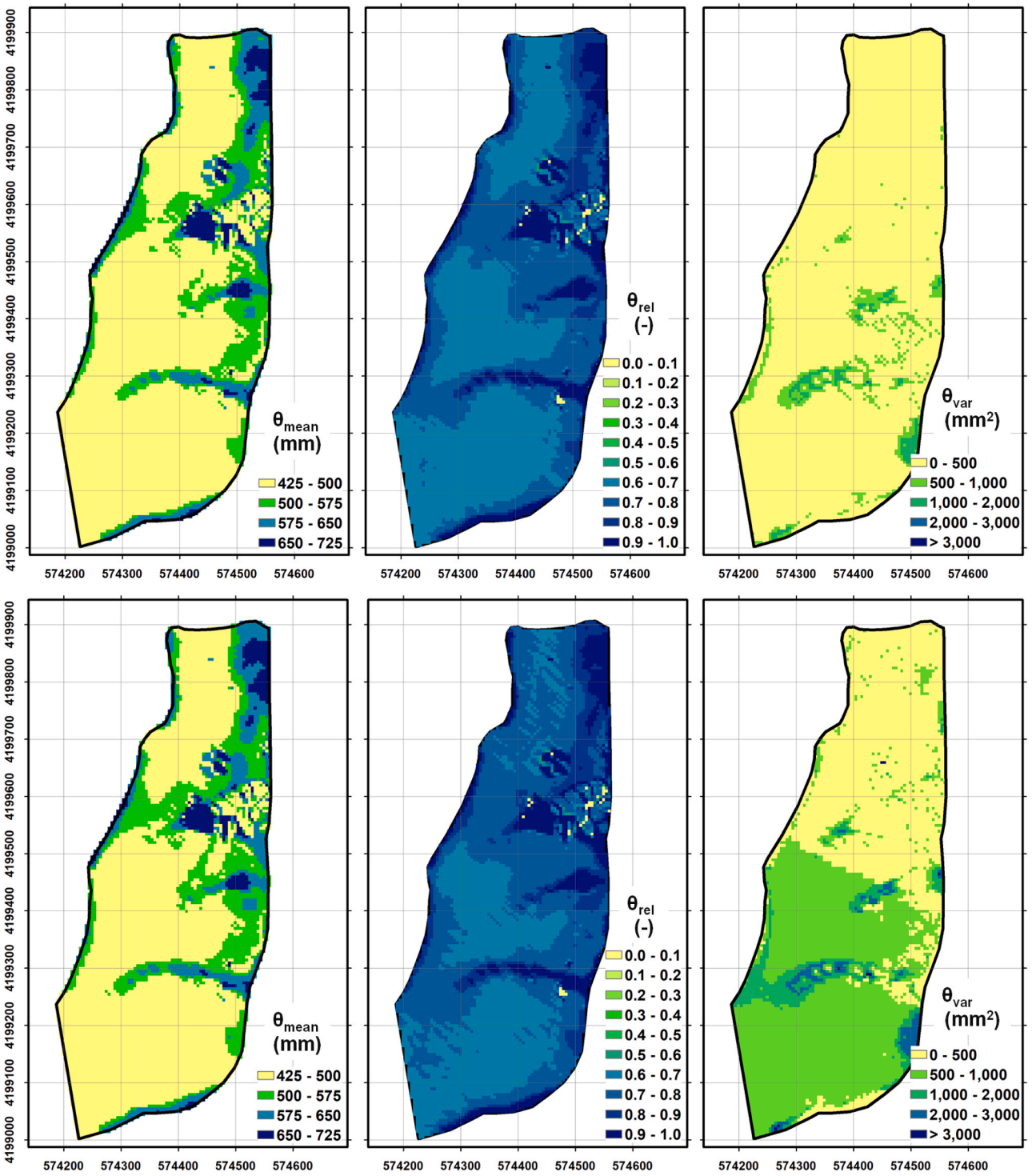

Fig. 9. Spatial distribution of the mean (θ_{mean}) and relative (θ_{rel}) soil water storage and variance of soil water storage simulations (θ_{var}) in 2019 (top) and 2020 (bottom).

The errors of the used PTFs were assumed to greatly influence the agreement between model simulations and soil moisture measurements taken at P1 and P2, resulting RMSE of 0.124 and 0.155 cm^3 cm^{-3}, respectively (Fig. 10). However, most of the error appeared to be systematic PTFs, since the difference between measurements and estimates could be averaged to 0.12 (P1) and 0.15 (P2) cm^3 cm^{-3} for the different soil depths and along both crop seasons. By reducing these systematic errors, e.g., with more accurate PTFs, RMSE of 0.035 and 0.029 cm^3 cm^{-3} could be obtained at P1 and P2, which correspond mainly to the random errors of both datasets. Such RMSE values are comparable to those obtained in 1D applications of the MOHID-Land model (Ramos et al., 2017, 2018, 2021; Simionesei et al., 2018). To unravel this issue further, a functional assessment of the regional PTFs should be performed, namely for α and K_s, which might justify the noted deviation between measured and simulated values.

As shown in Fig. 10, the simulated soil water content in both P1 and P2 was kept close to saturation during both growing seasons, which is consistent with the θ_{rel} maps (Fig. 9). This condition did not affect crop

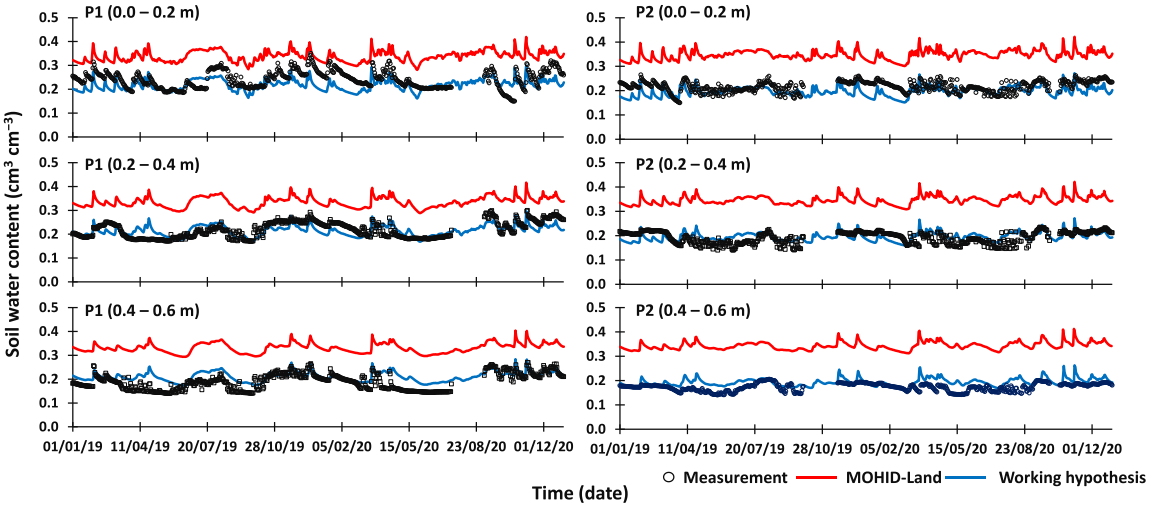

Fig. 10. Evolution of measured and simulated soil water contents in P1 and P2. The working hypothesis refers to the systematic errors (soil water content constant gap of 0.12–0.15 cm^3 cm^{-3}) that are associated with the regional PTFs used.

evapotranspiration estimates, with $T_a = T_p$ in most of the field, i.e., no water stress was observed in these areas. However, the seasonal T_a estimated by MOHID-Land (about 340 mm in both seasons) was much lower than the T_a obtained with SIMDualKc (377–655 mm; Ramos et al., 2023a) and HYDRUS-1D (593–648 mm; Ramos et al., 2023b) for the same study area and growing seasons. The latter estimates were calibrated and validated using soil water balance approaches. On the other hand, the adopted K_c and the ET_c values for the different crop stages (Table 2) agreed quite well with those estimated by Ramos et al. (2023a) for the almond orchard using the dual-K_c approach (Allen et al., 1998, 2005). The low T_a (and T_p) values obtained with MOHID-Land can therefore be attributed to the vegetation parameters affecting the partitioning of the ET_c into T_p and E_p during the crop season, i.e., the parameters describing the development of LAI. Also, the value of accumulated heat units used to describe the whole growing season affected those estimates. As no calibrated parameters for almond crop growth were available for the study region, the values used in this study were taken from the literature (Neitsch et al., 2011), leading to the underestimation of the length of the crop season and the seasonal T_a values. Therefore, a better assessment of crop growth parameters is essential to improve the reliability of model estimates. This becomes even more important when considering the complexity and the variability observed in orchard systems where surfaces are heterogeneous, the soil is incompletely covered, and varying planting density, canopy height, training system, inter-row management and irrigation management affect the amount of energy available for both the transpiration and soil evaporation processes and soil water fluxes (Pereira et al., 2020b; Volschenk, 2020; Fereres et al., 2012). The same limitations have already been reported when using MOHID-Land for grapevine in southern Portugal (Ramos et al., 2021).

Water that was not used by the crop eventually evaporated or percolated to depths below the root zone. Since crop water use was lower than that determined by Ramos et al. (2023a,b), the seasonal percolation was higher. Besides crop water use, seasonal percolation was also influenced by the division of precipitation into surface runoff and water infiltration. Vereecken et al. (2019) have detailed all the factors that influence the infiltration process in soils. In MOHID-Land, infiltration was estimated by solving the Richards equation, and was thus dependent on soil moisture conditions in the surface layer. These conditions were maintained high throughout simulations because of factors such as the coarse vertical discretization in the soil domain that further influenced the infiltration process. Furthermore, the soil hydraulic conductivity data used to generate PTFs were limited and did not reflect the flow conditions at the land surface - atmosphere interface, mainly because they were derived from measurements on soil cylinders collected below the soil surface; thus, not affected by soil crusting. This may have led to higher simulated values of infiltration and percolation than in reality. Other factors such as the temporal resolution of precipitation data (daily) influenced the partition of precipitation data. For instance, Batalha et al. (2018) demonstrated how using hourly meteorological data can lead to significantly different results in infiltration and runoff calculations compared to using data averaged over daily, weekly, monthly, and yearly timeframes. Since no significant runoff is expected from drip irrigation, the observed *RO* values were mainly a result from rainfall. Due to the use of daily precipitation data, the *RO* values were likely underestimated.

Model validation attempts to correlate the spatial distribution of T_a and biomass with maps of NDVI were inconclusive, with positive and negative correlations observed in 2019 and 2020, respectively. Despite correlations were considered significant at $P < 0.01$ for most of the available images, the Pearson correlation coefficients were less than 0.26 and greater than − 0.20 in 2019 and 2020, respectively. These low correlations are explained by the dynamics of grass and weeds in the field, which cannot be simulated by the MOHID-Land model. In 2019, the best positive correlations were found in March, during the winter dry season, when the presence of weeds was probably lowest. In 2020, the best negative correlations were found in June (Fig. S4). As the year was wetter in 2020, more weeds grew along waterlines and in the lower parts of the field where the model predicted water accumulation and wetter soil conditions. These had a large impact on NDVI, while MOHID-Land simply considered these areas unsuitable for crop development, returning a negative correlation with NDVI.

Despite the obvious difficulties in fully validating model results, this application demonstrates that EMI sensing can be useful in indirectly mapping spatial variability in soil properties (Taylor et al., 2003; King et al., 2005; Kelley et al., 2017), which is useful in precision agriculture for crop management planning, agrochemical applying, and irrigation scheduling. It also improves knowledge of soil water dynamics and identifies preferred flow paths at the field scale. Literature shows that EMI data have already been used to identify preferred pathways at the field scale (Zhu and Lin, 2009; Zhu et al., 2010; Triantafilis et al., 2013b; Doolittle et al., 2013), usually by assigning corridors or lines of higher EC_a to concentrations of seepage plums. EMI data has also been integrated with physical-based models to simulate the spatial variability of soil water dynamics, crop growth, and yields across management zones (Brogi et al., 2021, 2020; Wallor et al., 2019). As far as we know, EMI data have not yet been used with a distributed three-dimensional model to simulate soil water dynamics at field scale. In this study, the

integration of EMI data and three-dimensional modeling has helped to define a conceptual model of water dynamics at the field scale, that may ultimately be useful for defining better management practices to control soil erosion, runoff, and nutrient leaching from the study field.

Guo and Lin (2018) used a literature review to precisely define the factors affecting preferential flow at different scales. On the almond field, soil heterogeneity (soil texture and soil hydraulic properties), topography, and water input characteristics (precipitation regime and irrigation method) were identified as dominant factor affecting preferential flow. Soil stratification/structure (including soil cracks) and soil management could probably also be important controlling factors, but they could not be identified in the model simulations. The former because no information on soil structure was provided to the model with the assumed PTFs. The latter because the MOHID-Land model is still far from such advances.

4. Conclusions

This study aimed to evaluate the spatial variability of the soil water balance and fluxes at the field scale using the distributed model MOHID-Land. An EMI survey was performed over a 22.6-ha almond field and the inverted soil conductivity model was then related to the total sand and clay contents and used to calculate maps of soil hydraulic parameters. The model was used to simulate soil water dynamics at the field scale during two growing seasons (2019 and 2020). Maps were calculated with the spatial distribution of the components of the soil water balance, namely actual crop transpiration (T_a), actual soil evaporation (E_a), percolation below the root zone (DP), and surface runoff (RO). Maps of soil water contents were also calculated.

The results of the three-dimensional hydrological model made it possible to identify the areas more suitable for crop development and the preferred flow paths at the field scale. The main control factors influencing preferential flow paths were also identified, namely soil heterogeneity, topography, and water input characteristics. Despite justifying some estimates, these results were subject to considerable uncertainty, mainly due to limitations in characterizing soil hydraulic properties using available data and pedotransfer functions. Furthermore, the parametrization of the model (e.g., describing the crop growth process) and the coarse discretization of the soil domain were identified as factors that influenced the reliability of the estimates. As a result, certain areas requiring development were addressed and discussed. Nevertheless, there is a strong interest in further pursuing and improving a method that can enhance the combined use of EMI sensing and distributed modelling. Such contributions are of particular interest to the field of precision agriculture.

Declaration of Competing Interest

The authors declare that they have no known competing financial interests or personal relationships that could have appeared to influence the work reported in this paper.

Data Availability

Data will be made available on request.

Acknowledgments

This research project was supported by FCT/MCTES (PIDDAC) through project LARSyS–FCT Pluriannual funding 2020–2023 (UIDP/EEA/50009/2020), project SOIL4EVER (PTDC/ASP-SOL/28796/2017), and project HYDROVAR (2022.03921. PTDC). The support of FCT through grants attributed to T. B. Ramos (CEECIND/01152/2017) and H. Darouich (CEECIND/01153/2017) is also acknowledged.

Appendix A. Supporting information

Supplementary data associated with this article can be found in the online version at doi:10.1016/j.agwat.2023.108472.

References

Allen, R.G., Pereira, L.S., Raes, D., Smith, M., 1998. Crop Evapotranspiration – Guidelines for Computing Crop Water Requirements. In: Irrig. Drain. Paper, 56.. FAO, Rome, Italy.

Allen, R.G., Pereira, L.S., Smith, M., Raes, D., Wright, J.L., 2005. FAO-56 dual crop coefficient method for estimating evaporation from soil and application extensions. J. Irrig. Drain. Eng. 131 (1), 2–13. https://doi.org/10.1061/(ASCE)0733-9437(2005)131:1(2).

Allred, B., Daniels, J.J., Ehsani, M.R., 2008. Handbook of Agricultural Geophysics. CRC Press, Boca Raton, p. 423. https://doi.org/10.1201/9781420019353.

American Society of Civil Engineers (ASCE), 1996. Hydrology Handbook Task Committee on Hydrology Handbook; II Series, GB 661.2. H93. ASCE,, Reston, VA, USA, pp. 96–104.

Batalha, M.S., Barbosa, M.C., Faybishenko, B., van Genuchten, M.Th, 2018. Effect of temporal averaging of meteorological data on predictions of groundwater recharge. J. Hydrol. Hydromech. 66, 143–152. https://doi.org/10.1515/johh-2017-0051.

Brogi, C., Huisman, J.A., Weihermüller, L., Herbst, M., Vereecken, H., 2021. Added value of geophysics-based soil mapping in agro-ecosystem simulations. Soil 7 (1), 125–143. https://doi.org/10.5194/soil-7-125-2021.

Brogi, C., Huisman, J.A., Pätzold, S., von Hebel, C., Weihermüller, L., Kaufmann, M.S., van der Kruk, J., Vereecken, H., 2019. Large-scale soil mapping using multi-configuration EMI and supervised image classification. Geoderma 335 (1), 133–148. https://doi.org/10.1016/j.geoderma.2018.08.001.

Brogi, C., Huisman, J.A., Herbst, M., Weihermüller, L., Klosterhalfen, A., Montzka, C., Reichenau, T.G., Vereecken, H., 2020. Simulation of spatial variability in crop leaf area index and yield using agroecosystem modeling and geophysics-based quantitative soil information. Vadose Zone J. 19, e20009 https://doi.org/10.1002/uar2.20009.

Cockx, L., Van Meirvenne, M., Vitharana, U.W.A., Verbeke, L.P.C., Simpson, D., Saey, T., Van Coille, F.M.B., 2009. Extracting topsoil information from EM38DD sensor data using neural network approach. Soil Sci. Soc. Am. J. 73 (6), 1–8. https://doi.org/10.2136/sssaj2008.0277.

Copernicus, 2023. Copernicus Open Access Hub. European Commission (Last accessed 15.02.2023).

Corwin, D.L., Lesch, S.M., 2005. Characterizing soil spatial variability with apparent soil electrical conductivity: I. Survey protocols. Comput. Electron. Agric. 46, 103–133. https://doi.org/10.1016/j.compag.2004.11.002.

Dane, J.H., Hopmans, J.W., 2002. Pressure plate extractor. In: Dane, J.H., Topp, G.C. (Eds.), Methods of Soil Analysis, Part 4, Physical Methods. Soil Science Society of America Book Series. Soil Science Society of America, Madison, Wisconsin, pp. 688–690.

DeGroot-Hedlin, C., Constable, S.C., 1990. Occam's inversion to generate smooth, two dimensional models from magnetotelluric data. Geophysics 55, 1613–1624. https://doi.org/10.1190/1.1442813.

Doolittle, J., Chibirka, J., Muñiz, E., Shaw, R., 2013. Using EMI and P-XRF to characterize the magnetic properties and the concentration of metals in soils formed over different lithologies. Soil Horiz. 54, 1–10. https://doi.org/10.2136/sh13-01-0009.

Doolittle, J.A., Brevik, E.C., 2014. The use of electromagnetic induction techniques in soils studies. Geoderma 223–225, 33–45. https://doi.org/10.1016/j.geoderma.2014.01.027.

Dragonetti, G., Farzamian, M., Basile, A., Monteiro Santos, F., Coppola, A., 2022. In situ estimation of soil hydraulic and hydrodispersive properties by inversion of electromagnetic induction measurements and soil hydrological modelling. Hydrol. Earth Syst. Sci. 26, 5119–5136. https://doi.org/10.5194/hess-26-5119-2022.

Farzamian, M., Ribeiro, J.A., Monteiro Santos, F.A., Khalil, M.A., 2019. Application of transient electromagnetic and audio-magnetotelluric methods for imaging the monte real aquifer in Portugal. Pure Appl. Geophys. 176, 719–735. https://doi.org/10.1007/s00024-018-2030-7.

Farzamian, M., Autovino, D., Basile, A., De Mascellis, R., Dragonetti, G., Monteiro Santos, F., Binley, A., Coppola, A., 2021. Assessing the dynamics of soil salinity with time-lapse inversion of electromagnetic data guided by hydrological modelling. Hydrol. Earth Syst. Sci. 25, 1509–1527. https://doi.org/10.5194/hess-25-1509-2021.

Farzamian, M., Bouksila, F., Paz, Monteiro, Santos, F., A, Zemin, N., Salma, F., Ben Slimane, A., Selimi, T., Triantafilis, J., 2023. Landscape-scale mapping of soil salinity with multi-height electromagnetic induction and quasi-3D inversion (Saharan Oasis, Tunisia). Agric. Water Manag. 284, 108330 https://doi.org/10.1016/j.agwat.2023.108330.

Fatichi, S., Vivoni, E.R., Ogden, F.L., Ivanov, V.Y., Mirus, B., Gochis, D., Downer, C.W., Camporese, M., Davison, J.H., Ebel, B., Jones, N., Kim, J., Mascaro, G., Niswonger, R., Restrepo, P., Rigon, R., Shen, C., Sulis, M., Tarboton, D., 2016. An overview of current applications, challenges, and future trends in distributed process-based models in hydrology. J. Hydrol. 537, 45–60. https://doi.org/10.1016/J.JHYDROL.2016.03.026.

Feddes, R.A., Kowalik, P.J., Zaradny, H., 1978. Simulation of Field Water Use and Crop Yield. Simulation Monographs Pudoc, Wageningen, The Netherlands.

Fereres, E., Goldhamer, D., Sadras, V., Smith, M., Marsal, J., Girona, J., Naor, A., Gucci, R., Caliandro, A., Ruz, C., 2012. Yield response to water of fruit trees and vines: guidelines. In: Steduto, P., Hsiao, T., Fereres, E., Raes, D. (Eds.), Crop yield response to water. FAO Irrigation and Drainage Paper N°. 66. Food and Agriculture Organization of the United Nations, Rome.

Gee, G.W., Or, D., 2002. Particle size analysis. In: Dane, J.H., Topp, G.C. (Eds.), Methods of Soil Analysis, Part 4, Physical Methods. Soil Science Society of America Book Series. Soil Science Society of America, Madison, Wisconsin, pp. 255–294.

Gomes, M.P., Silva, A.A., 1962. Um novo diagrama triangular para a classificação básica da textura do solo. Garcia Orta 10, 171–179.

Gómez Flores, J.L., Ramos Rodríguez, M., González Jiménez, A., Farzamian, M., Herencia Galán, J.F., Salvatierra Bellido, B., Cermeño Sacristan, P., Vanderlinden, K., 2022. Depth-specific soil electrical conductivity and NDVI elucidate salinity effects on crop development in reclaimed marsh soils. Remote Sens 14, 3389. https://doi.org/10.3390/rs14143389.

Gonçalves, M.C., Ramos, T.B., Pires, F.P., 2011. Base de dados georreferenciada das propriedades do solo. In: Coelho, P.S., Reis, P. (Eds.), Agrorrural. Contributos Científicos. Instituto Nacional dos Recursos Biológicos. I.P. e Imprensa Nacional – Casa da Moeda, S.A., Portugal, pp. 564–574.

González Jiménez, A., Pachepsky, Y., Gómez Flores, J.L., Ramos Rodríguez, M., Vanderlinden, K., 2022. Correcting on-the-go field measurement–coordinate mismatch by minimizing nearest neighbor difference. Sensors 22 (4), 1496. https://doi.org/10.3390/s22041496.

Guo, L., Lin, H., 2018. Addressing two bottlenecks to advance the understanding of preferential flow in soils. Adv. Agron. 147, 61–117. https://doi.org/10.1016/bs.agron.2017.10.002.

Hersbach, H., Bell, B., Berrisford, P., Biavati, G., Horányi, A., Muñoz Sabater, J., Nicolas, J., Peubey, C., Radu, R., Rozum, I., Schepers, D., Simmons, A., Soci, C., Dee, D., Thépaut, J.-N., 2018. ERA5 hourly data on single levels from 1979 to present. Copernicus Climate Change Service (C3S) Climate Data Store (CDS). (Accessed on 04–01-2022), https://doi.org/10.24381/cds.adbb2d47.

Horta, A., Oliveira, A.R., Azevedo, L., Ramos, T.B., 2023. Using digital soil hydraulic properties maps to simulate soil-water balance – implications for water management plans. Geoderma Reg. (in preparation).

Huang, J., Monteiro Santos, F.A., Triantafilis, J., 2016. Mapping soil water dynamics and a moving wetting front by spatiotemporal inversion of electromagnetic induction data. Water Resour. Res. 52 (11), 9131–9145. https://doi.org/10.1002/2016WR019330.

Huang, J., Lark, R.M., Robinson, D.A., Lebron, I., Keith, A.M., Rawlins, B., Tye, A., Kuras, O., Raines, M., Triantafilis, J., 2014. Scope to predict soil properties at within-field scale from small samples using proximally sensed γ-ray spectrometer and EM induction data. Geoderma 232–234, 69–80. https://doi.org/10.1016/j.geoderma.2014.04.031.

IUSS Working Group WRB, 2014. World Reference Base for Soil Resources 2014. International Soil Classification System for Naming Soils and Creating Legends for Soil Maps. World Soil Resources Reports No. 106. FAO, Rome.

Jayawickreme, D.H., Jobbágy, E.G., Jackson, R.B., 2014. Geophysical subsurface imaging for ecological applications. N. Phytol. 201, 1170–1175. https://doi.org/10.1111/nph.12619.

Kelley, J., Higgins, C.W., Pahlow, M., Noller, J., 2017. Mapping soil texture for electromagnetic induction: a case for regional data coordination. Soil Sci. Soc. Am. J. 81, 923–931. https://doi.org/10.2136/sssaj2016.12.0432.

King, J.A., Dampney, P.M.R., Lark, R.M., Wheeler, H.C., Bradley, R.I., Mayr, T.R., 2005. Mapping potential crop management zones within fields: use of yield-map series and patterns of soil physical properties identified by electromagnetic induction sensing. Precis. Agric. 6, 167–181. https://doi.org/10.1007/s11119-005-1033-4.

Legates, D., McCabe, G., 1999. Evaluating the use of goodness of fit measures in hydrologic and hydroclimatic model validation. Water Resour. Res. 35, 233–241. https://doi.org/10.1029/1998WR900018.

Lin, L.I.-K., 1989. A concordance correlation coefficient to evaluate reproducibility. Biometrics 45, 255–268. https://doi.org/10.2307/2532051.

Martinez, G., Huang, J., Vanderlinden, K., Giráldez, J.V., Triantafilis, J., 2018. Potential to predict depth-specific soil-water content beneath an olive tree using electromagnetic conductivity imaging. Soil Use Manag 34 (2), 236–248. https://doi.org/10.1111/sum.12411.

McBride, G.B., 2005. A proposal for strength-of-agreement criteria for Lin's concordance correlation coefficient. NIWA Client Rep. 45, 307–310. HAM2005–062.

Melich, A., 1948. Determination of cations and anions exchange properties of soils. Soil Sci. 66, 429–446.

Mohanty, B.P., 2013. Soil hydraulic property estimation using remote sensing: a review. Vadose Zone J. 12 (4), 1–9. https://doi.org/10.2136/vzj2013.06.0100.

Monteiro Santos, F.A., 2004. 1-D laterally constrained inversion of EM34 profiling data. J. Appl. Geophys. 56 (2), 123–134. https://doi.org/10.1016/j.jappgeo.2004.04.005.

Monteiro Santos, F.A., Triantafilis, J., Bruzgulis, K.E., Roe, J.A.E., 2010. Inversion of multiconfiguration electromagnetic (DUALEM-421S) profiling data using a one-dimensional laterally constrained algorithm. Vadose Zone J. 9, 117–125. https://doi.org/10.2136/vzj2009.0088.

Mualem, Y., 1976. A new model for predicting the hydraulic conductivity of unsaturated porous media. Water Resour. Res. 12, 513–522. https://doi.org/10.1029/WR012i003p00513.

Nawar, S., Corstanje, R., Halcro, G., Mulla, D., Mouazen, A.M., 2017. Delineation of soil management zones for variable-rate fertilization. A Rev. Adv. Agron. 143, 175–245. https://doi.org/10.1016/bs.agron.2017.01.003.

Neitsch, S.L., Arnold, J.G., Kiniry, J.R., Williams, J.R., 2011. Soil and Water Assessment Tool. Theoretical documentation, version 2009. Texas Water Resources Institute. Technical Report nº 406. Texas A&M University System, College Station, Tx.

Nelson, D.W., Sommers, L.E., 1982. Total carbon, organic carbon, and organic matter. In: Page, A.L., et al. (Eds.), Methods of Soil Analysis. Part 2. Chemical and Microbiological Properties. Agron. Monogr. 9. ASA and SSSA, Madison, WI, pp. 539–579.

Oliveira, A.R., Ramos, T.B., Simionesei, L., Pinto, L., Neves, R., 2020. Sensitivity analysis of the MOHID-land hydrological model: a case study of the Ulla River Basin. Water 12, 3258. https://doi.org/10.3390/w12113258.

Paz, A.M., Castanheira, N., Farzamian, M., Paz, M.C., Gonçalves, M.C., Monteiro Santos, F.A., Triantafilis, J., 2020. Prediction of soil salinity and sodicity using electromagnetic conductivity imaging. Geoderma 361, 114086. https://doi.org/10.1016/j.geoderma.2019.114086.

Pereira, L.S., Cordery, I., Iacovides, I., 2009. Coping with Water scarcity. Addressing the Challenges. Springer, Dordrecht, p. 382.

Pereira, L.S., Paredes, P., Jovanovic, N., 2020a. Soil water balance models for determining crop water and irrigation requirements and irrigation scheduling focusing on the FAO56 method and the dual Kc approach. Agric. Water Manag. 241, 106357 https://doi.org/10.1016/j.agwat.2020.106357.

Pereira, L.S., Paredes, P., Melton, F., Johnson, L., Wang, T., López-Urrea, R., Cancela, J. J., Allen, R., 2020b. Prediction of crop coefficients from fraction of ground cover and height. Background and validation using ground and remote sensing data. Agric. Water Manag. 241, 106197 https://doi.org/10.1016/j.agwat.2020.106197.

Phogat, V., Pitt, T., Cox, J.W., Šimůnek, J., Skewes, M.A., 2018. Soil water and salinity dynamics under sprinkler irrigated almond exposed to a varied salinity stress at different growth stages. Agric. Water Manag. 201, 70–82. https://doi.org/10.1016/j.agwat.2018.01.018.

Rallo, G., Paço, T.A., Paredes, P., Puig-Sirera, À., Massai, R., Provenzano, G., Pereira, L. S., 2021. Updated single and dual crop coefficients for tree and vine fruit crops. Agric. Water Manag. 250, 106645 https://doi.org/10.1016/j.agwat.2020.106645.

Ramos, T.B., Darouich, H., Gonçalves, M.C., 2023c. Development and functional evaluation of pedotransfer functions for estimating soil hydraulic properties in Portuguese soils: implications for soil water Dynamics. Geoderma Reg. (in preparation).

Ramos, T.B., Gonçalves, M.C., Martins, J.C., Pereira, L.S., 2014b. Comparação de diferentes funções de pedotransferência para estimar as propriedades hidráulicas dos solos em Portugal. In: Gonçalves, M.C., Ramos, T.B., Martins, J.C. (Eds.), Livro de Actas do Encontro Anual da Sociedade Portuguesa da Ciência do Solo, 26 to 28 June. Instituto Nacional de Investigação Agrária e Veterinária, Oeiras, pp. 29–34.

Ramos, T.B., Gonçalves, M.C., Brito, D., Martins, J.C., Pereira, L.S., 2013. Development of class pedotransfer functions for integrating water retention properties into Portuguese soil maps. Soil Res 51, 262–277. https://doi.org/10.1071/SR12347.

Ramos, T.B., Horta, A., Gonçalves, M.C., Martins, J.C., Pereira, L.S., 2014a. Development of ternary diagrams for estimating water retention properties using geostatistical approaches. Geoderma 230–231, 229–242. https://doi.org/10.1016/j.geoderma.2014.04.017.

Ramos, T.B., Simionesei, L., Jauch, E., Almeida, C., Neves, R., 2017. Modelling soil water and maize growth dynamics influenced by shallow groundwater conditions in the Sorraia Valley region, Portugal. Agric. Water Manag. 185, 27–42. https://doi.org/10.1016/j.agwat.2017.02.007.

Ramos, T.B., Simionesei, L., Oliveira, A.R., Darouich, H., Neves, R., 2018. Assessing the impact of LAI data assimilation on simulations of the soil water balance and maize development using MOHID-Land. Water 10, 1367. https://doi.org/10.3390/w10101367.

Ramos, T.B., Simionesei, L., Oliveira, A.R., Neves, R., Darouich, H., 2021. Exploring the use of vegetation indices for validating crop transpiration fluxes computed with the MOHID-Land model. Application to vineyard. Agronomy 11, 1228. https://doi.org/10.3390/agronomy11061228.

Ramos, T.B., Darouich, H., Oliveira, A.R., Farzamian, M., Monteiro, T., Castanheira, N., Paz, A., Gonçalves, M.C., Pereira, L.S., 2023a. Water use and soil water balance of Mediterranean tree crops assessed with the SIMDualKc model in orchards of southern Portugal. Agric. Water Manag. 279, 108209 https://doi.org/10.1016/j.agwat.2023.108209.

Ramos, T.B., Darouich, H., Oliveira, A.R., Farzamian, M., Monteiro, T., Castanheira, N., Paz, A., Alexandre, C., Gonçalves, M.C., Pereira, L.S., 2023b. Water use, soil water balance and soil salinization risks of Mediterranean tree orchards in southern Portugal under current climate variability: Issues for salinity control and irrigation management. Agric. Water Manag. 283, 108319 https://doi.org/10.1016/j.agwat.2023.108319.

Ritchie, J.T., 1972. Model for predicting evaporation from a row crop with incomplete cover. Water Resour. Res. 8, 1204–1213. https://doi.org/10.1029/WR008i005p01204.

Romano, N., Hopmans, J.W., Dane, J.H., 2002. Suction table. In: Dane, J.H., Topp, G.C. (Eds.), Methods of Soil Analysis, Part 4, Physical Methods. Soil Science Society of America Book Series. Soil Science Society of America, Madison, Wisconsin, pp. 692–698.

Rouse, J., Haas, R., Schell, J., Deering, D., 1973. Monitoring vegetation systems in the Great plains with ERTS. Third ERTS Symposium. NASA SP-351, pp. 309–317.

Sasaki, Y., 2001. Full 3-D inversion of electromagnetic data on PC. J. Appl. Geophys. 46, 45–54. https://doi.org/10.1016/S0926-9851(00)00038-0.

Simionesei, L., Ramos, T.B., Oliveira, A.R., Jongen, M., Darouich, H., Weber, K., Proença, V., Domingos, T., Neves, R., 2018. Modeling soil water dynamics and pasture growth in the montado ecosystem using MOHID-Land. Water 10, 489. https://doi.org/10.3390/w10040489.

Šimůnek, J., Hopmans, J.W., 2009. Modeling compensated root water and nutrient uptake. Ecol. Model. 220, 505–521. https://doi.org/10.1016/j.ecolmodel.2008.11.004.

Šimůnek, J., Genuchten, M.Th, Šejna, M., 2008. Development and applications of the HYDRUS and STANMOD software packages and related codes. Vadose Zone J. 7 (2), 587–600. https://doi.org/10.2136/VZJ2007.0077.

Šimůnek, J., Genuchten, M.Th, Šejna, M., 2016. Recent developments and applications of the HYDRUS computer software packages. Vadose Zone J. 15 (7), 1–25. https://doi.org/10.2136/VZJ2016.04.0033.

Skaggs, T.H., van Genuchten, M.Th, Shouse, P.J., Poss, J.A., 2006. Macroscopic approaches to root water uptake as a function of water and salinity stress. Agric. Water Manag. 86, 140–149. https://doi.org/10.1016/j.agwat.2006.06.005.

Taylor, J.C., Wood, G.A., Earl, R., Godwing, R.J., 2003. Soil factors and their influence on within-field crop variability, Part II: Spatial analysis and determination of management zones. Biosyst. Eng. 84 (4), 441–453. https://doi.org/10.1016/S1537-5110(03)00005-9.

Trancoso, A.R., Braunschweig, F., Chambel-Leitão, P., Obermann, M., Neves, R., 2009. An advanced modelling tool for simulating complex river systems. Sci. Total Environ. 407, 3004–3016. https://doi.org/10.1016/j.scitotenv.2009.01.015.

Triantafilis, J., Terhune IV, C.H., Monteiro Santos, F.A., 2013a. An inversion approach to generate electromagnetic conductivity images from signal data. Environ. Model. Softw. 43, 88–95. https://doi.org/10.1016/j.envsoft.2013.01.012.

Triantafilis, J., Lesch, S., Lau Lau, K., Buchanan, S., 2009. Field level digital soil mapping of cation exchange capacity using electromagnetic induction and a hierarchical spatial regression model. Aust. J. Soil Res. 47, 651–663. https://doi.org/10.1071/SR08240.

Triantafilis, J., Ribeiro, J., Page, D., Santos, F.A.M., 2013b. Inferring the location of preferential flow paths of a leachate plume by using a DUALEM-421 and a quasi-three-dimensional inversion model. Vadose Zone J. 12, 1–11. https://doi.org/10.2136/vzj2012.0086.

UNESCO, 2020. United Nations World Water Development Report 2020. Water and Climate Change. UNESCO, Paris.

U.S. Salinity Laboratory Staff, 1954. Diagnosis and improvement of saline and alcaly soils. USDA Handbook 60, Washington, USA.

van Dam, J.C., De Rooij, G., Heinen, M., Stagnitti, F., 2004. Concepts and dimensionality in modeling unsaturated water flow and solute transport. In: Feddes, R., de Rooij, G., van Dam, J. (Eds.), Unsaturated-zone modeling: progress, challenges and applications. Kluwer Academic, Dordrecht, Netherlands, pp. 1–36.

van der Sande, C.J., de Jong, S.M., de Roo, A.P.J., 2003. A segmentation and classification approach of IKONOS-2 imagery for land cover mapping to assist flood risk and flood management assessment. Int. J. Appl. Earth Obs. Geoinf. 4, 217–229. https://doi.org/10.1016/S0303-2434(03)00003-5.

van Genuchten, M.Th, 1980. A closed form equation for predicting the hydraulic conductivity of unsaturated soils. Soil Sci. Soc. Am. J. 44, 892–898. https://doi.org/10.2136/sssaj1980.03615995004400050002x.

Van Looy, K., Bouma, J., Herbst, M., Koestel, J., Minasny, B., Mishra, U., Montzka, C., Nemes, A., Pachepsky, Y.A., Padarian, J., Schaap, M.G., Tóth, B., Verhoef, A., Vanderborght, J., van der Ploeg, M.J., Weihermüller, L., Zacharias, S., Zhang, Y., Vereecken, H., 2017. Pedotransfer functions in earth system science: challenges and perspectives. Rev. Geophys. 55 (4), 1199–1256. https://doi.org/10.1002/2017RG000581.

Vereecken, H., Kasteel, R., Vanderborght, J., Harter, T., 2007. Upscaling hydraulic properties and soil water flow processes in heterogeneous soils: a review. Vadose Zone J. 6 (1), 1–28. https://doi.org/10.2136/VZJ2006.0055.

Vereecken, H., Amelung, W., Bauke, S.L., Bogena, H., Brüggemann, N., Montzka, C., Vanderborght, J., Bechtold, M., Blöschl, G., Carminati, A., Javaux, M., Konings, A.G., Kusche, J., Neuweiler, I., Or, D., Steele-Dunne, S., Verhoef, A., Young, M., Zhang, Y., 2022. Soil hydrology in the earth system. Nat. Rev. Earth Environ. 3 (9), 573–587. https://doi.org/10.1038/s43017-022-00324-6.

Vereecken, H., Weihermüller, L., Assouline, S., Šimůnek, J., Verhoef, A., Herbst, M., Archer, N., Mohanty, B., Montzka, C., Vanderborght, J., Balsamo, G., Bechtold, M., Boone, A., Chadburn, S., Cuntz, M., Decharme, B., Ducharne, A., Ek, M., Garrigues, S., Görgen, K., Ingewersen, J., Kollet, S., Lawrence, D.M., Li, Q., Or, D., Swenson, S., de Vrese, P., Walko, R., Wu, Y., Xue, Y., 2019. Infiltration from the pedon to global grid scales: an overview and outlook for land surface modelling. Vadose Zone J. 18, 18019. https://doi.org/10.2136/vzj2018.10.0191.

Volschenk, T., 2020. Water use and irrigation management of pomegranate trees - a review. Agric. Water Manag. 241, 106375 https://doi.org/10.1016/j.agwat.2020.106375.

Wallor, E., Kersebaum, K.C., Lorenz, K., Gebbers, R., 2019. Soil state variables in space and time: first steps towards linking proximal soil sensing and process modelling. Precis. Agric. 20, 313–334. https://doi.org/10.1007/s11119-018-9617-y.

Weihermüller, L., Lehmann, P., Herbst, M., Rahmati, M., Verhoef, A., Or, D., Jacques, D., Vereecken, H., 2021. Choice of pedotransfer functions matters when simulating soil water balance fluxes. J. Adv. Model. Earth Syst. 13, e2020MS002404 https://doi.org/10.1029/2020MS002404.

Williams, J.R., Jones, C.A., Kiniry, J.R., Spanel, D.A., 1989. The EPIC crop growth model. Trans. ASAE 32, 497–511. https://doi.org/10.13031/2013.31032.

Wösten, J.H.M., Pachepsky, Y.A., Rawls, W.J., 2001. Pedotransfer functions: bridging the gap between available basic soil data and missing soil hydraulic characteristics. J. Hydrol. 251, 123–150. https://doi.org/10.1016/S0022-1694(01)00464-4.

Zare, E., Li, N., Khongnawang, T., Farzamian, M., Triantafilis, J., 2020. Identifying potential leakage zones in an irrigation supply channel by mapping soil properties using electromagnetic induction, inversion modelling and a support vector machine. Soil Syst. 4 (2), 25. https://doi.org/10.3390/soilsystems4020025.

Zhu, Q., Lin, H.S., 2009. Simulation and validation of concentrated subsurface lateral flow paths in an agricultural landscape. Hydrol. Earth Syst. Sci. 13, 1503–1518. https://doi.org/10.5194/hess-13-1503-2009.

Zhu, Q., Lin, H., Doolittle, J., 2010. Repeated electromagnetic induction surveys for determining subsurface hydrologic dynamics in an agricultural landscape. Soil Sci. Soc. Am. J. 74, 1750–1762. https://doi.org/10.2136/sssaj2010.0055.